Electromagnetic wave fields in the microdiffraction domain

Román Castañeda*

Physics School, Universidad Nacional de Colombia Sede Medellín, A.A. 3840 Medellín, Colombia

(Received 8 September 2013; revised manuscript received 25 November 2013; published 29 January 2014)

Paraxial propagation theories are not suitable for describing the behavior of electromagnetic wave fields in any states of spatial coherence and polarization in the microdiffraction domain. The proposed nonparaxial theory overcomes such limitations by modeling (i) any planar source in terms of sets of point sources with tensor statistical behavior, and (ii) the transport of the wave field on scalar, deterministic, time-independent, and nonparaxial propagation modes, defined only by the geometry of the boundary conditions of the experimental setups. So the field emission by the source and the space structure due to the modes are independent from each other. The theory provides a unified framework for the power and the states of spatial coherence and polarization of the field, as well as for interference and diffraction, and describes the significant changes suffered by the wave fields in the microdiffraction domain.

DOI: 10.1103/PhysRevA.89.013843 PACS number(s): 42.25.Kb, 42.25.Bs, 42.25.Ja

I. INTRODUCTION

The term microdiffraction refers to the propagation of wave fields in the visible range, emitted by planar sources with sizes comparable to the wavelength along distances also comparable to the wavelength. A transport theory of electromagnetic wave fields in the microdiffraction domain is useful for the development of very compact optical devices at the micro- and nanoscales. Its mathematical formulation is also applicable to spectral ranges different from the visible, for which the term microdiffraction should be appropriately adapted. However, this work concerns the visible range, where the term is meaningful.

Nonparaxial diffraction theories of electromagnetic waves in the microdiffraction domain have established the vector formulation as an unavoidable requirement. It is fairly reviewed in [1] and references therein. Such theories concern the rigorous solution of Maxwell's equations for diffracting apertures of specific shapes (usually circular) and sizes, and discuss the validity of the Kirchhoff's boundary conditions in such contexts. However, they are usually mathematically intricate and computationally time consuming, so that their practical applicability is limited. Furthermore, they concern the propagation of the electric and magnetic field vectors but not their correlations, and therefore, they are not suitable for describing the microdiffraction of electromagnetic wave fields in any state of spatial coherence.

A tensor theory, named the second-order theory of electromagnetic spatial coherence, was developed to this aim [2]. It describes both the spatial coherence and the polarizations states of the electromagnetic wave field, on any specific plane, in terms of 2×2 tensors, named the (electric and magnetic) cross-spectral density tensors. Their elements are integral expressions obtained by solving the coupled Helmholtz equations for correlated electromagnetic wave fronts by the Green's function method under the boundary conditions specified by the experimental setup. By assuming random stationary electromagnetic wave fields in arbitrary states of spatial coherence and polarization, emitted by planar sources at the aperture plane (AP), the resulting integrals are the Wolf's type [2] and represent the nonparaxial propagation of the correlations between specific Cartesian components of the field vectors to the observation plane (OP).

This theory significantly gains in mathematical versatility without loss of accuracy by modeling the planar source in terms of a distribution of separate but inserted sets of radiant and virtual point sources [3], whose contributions are transported from the AP to the OP by means of a characteristic nonparaxial modal expansion [4]. It allows separating the physical attributes of the planar source from the spatial attributes of the propagation modes. Indeed, the emissions of the point sources are of a statistical nature and determine the power distribution and the states of spatial coherence and polarization of the wave field at the AP, while the nonparaxial modes are scalar, deterministic, and time-independent functions, defined by the boundary conditions of the setup for the whole region delimited by the AP and the OP. And the same set of modes is involved in the transport of all the physical attributes of the wave field. Thus the required tensor formulation can be treated in terms of a suitable set of scalar integral equations of the Wolf's type.

Nevertheless, this methodology implies more than the mathematical versatility. Novel attributes should be conferred to both the electromagnetic wave field and the space delimited by the setup in order to realize the physical meaning of its accurate predictions, as discussed below. The basic concepts and terminology are established in the references and are used directly.

II. THE NONPARAXIAL PROPAGATION

Because of the Maxwellian coupling between the electric and the magnetic field vectors [5], it is enough to develop the theory with basis on the electric cross-spectral density tensor [2]. The conceptual sketch in Fig. 1 shows the geometry used in this theory. The center-and-difference coordinates $(\boldsymbol{\xi}_A, \boldsymbol{\xi}_D)$ and $(\mathbf{r}_A, \mathbf{r}_D)$ univocally determine pairs of points $\boldsymbol{\xi}_\pm = \boldsymbol{\xi}_A \pm \boldsymbol{\xi}_D/2$ on the AP and $\mathbf{r}_\pm = \mathbf{r}_A \pm \mathbf{r}_D/2$ on the OP, and the axes x and y allow decomposing the electric field vectors in Cartesian components at both planes. The z axis is orthogonal to both the AP and the OP and determines the direction of propagation.

*Corresponding author: rcastane@unal.edu.co

 ©2014 American Physical Society

As deduced in the Appendix, the electric cross-spectral density tensor at the frequency ν, referred to these coordinates, becomes at the OP,

$$\mathbf{W}(\mathbf{r}_+,\mathbf{r}_-) = \int_{AP}\int_{AP} d^2\xi_A\, d^2\xi_D \;\; \boldsymbol{\Psi}(\boldsymbol{\xi}_+)\, \boldsymbol{\eta}(\boldsymbol{\xi}_+,\boldsymbol{\xi}_-)\, \boldsymbol{\Psi}(\boldsymbol{\xi}_-) \langle |E_0(\boldsymbol{\xi}_+)|^2\rangle^{\frac{1}{2}}\, \langle |E_0(\boldsymbol{\xi}_-)|^2\rangle^{\frac{1}{2}} \Phi(\boldsymbol{\xi}_+,\boldsymbol{\xi}_-;\mathbf{r}_+,\mathbf{r}_-;\lambda,z), \tag{1}$$

with the scalar kernel

$$\Phi(\boldsymbol{\xi}_+,\boldsymbol{\xi}_-;\mathbf{r}_+,\mathbf{r}_-;\lambda,z) = \left(\frac{k}{4\pi}\right)^2 t(\boldsymbol{\xi}_+)\, t^*(\boldsymbol{\xi}_-) \left(\frac{z+|\mathbf{z}+\mathbf{r}_A-\boldsymbol{\xi}_A+(\mathbf{r}_D-\boldsymbol{\xi}_D)/2|}{|\mathbf{z}+\mathbf{r}_A-\boldsymbol{\xi}_A+(\mathbf{r}_D-\boldsymbol{\xi}_D)/2|^2}\right)\left(\frac{z+|\mathbf{z}+\mathbf{r}_A-\boldsymbol{\xi}_A-(\mathbf{r}_D-\boldsymbol{\xi}_D)/2|}{|\mathbf{z}+\mathbf{r}_A-\boldsymbol{\xi}_A-(\mathbf{r}_D-\boldsymbol{\xi}_D)/2|^2}\right)$$
$$\times \exp(i\,k\,|\mathbf{z}+\mathbf{r}_A-\boldsymbol{\xi}_A+(\mathbf{r}_D-\boldsymbol{\xi}_D)/2| - i\,k\,|\mathbf{z}+\mathbf{r}_A-\boldsymbol{\xi}_A-(\mathbf{r}_D-\boldsymbol{\xi}_D)/2|), \tag{2}$$

where $k = 2\pi/\lambda$, $|\mathbf{z}| = z$, and $t(\boldsymbol{\xi}_\pm) = |\,t(\boldsymbol{\xi}_\pm)|\exp[\,i\,\varphi(\boldsymbol{\xi}_\pm)]$ is the complex value of the transmission at each point on the AP. The integrals in Eq. (1) are performed on each tensor element individually. The elements of the 2×2 tensors $\boldsymbol{\Psi}(\boldsymbol{\xi}_\pm)$ and $\boldsymbol{\eta}(\boldsymbol{\xi}_+,\boldsymbol{\xi}_-)$ are defined by Eqs. (A4) and (A5) in the Appendix. Their product in the integrand of Eq. (1) determines the states of spatial coherence and polarization of the electromagnetic wave field emitted by the planar source at the AP, which are of statistical nature. In contrast, the scalar kernel is time-independent, deterministic, and defined by the boundary conditions established by the experimental setup, for the complete volume between the AP and the OP, i.e., it is independent from the physical field features. Furthermore, it has no restrictions in numerical aperture, propagation distance, and sizes of both the planar source and the detector.

This kernel determines the nonparaxial modes [4] for the transport of the electromagnetic wave field, whose mathematical forms associated to specific field attributes (i.e., power, spatial coherence state, polarization state) are determined by evaluating their arguments. The parameter λ in k should be understood as a scale metric, i.e., the length established by the boundary conditions along which the argument of the kernel propagator in Eq. (2) evolves in 2π. The spatial scale metric is related to the wavelength of the electromagnetic field in such a way that the nonparaxial modes with specific λ transport the field of wavelength equal to λ. Likewise, the boundary conditions specify the values of $t(\boldsymbol{\xi}_\pm)$, which in turn determine the amplitude of the wave field emerging from each point $\boldsymbol{\xi}_\pm$.

Therefore the nonparaxial modes, defined by the kernel in Eq. (2), establish a spatial structure in the whole region of the setup delimited by the AP and the OP. It is in the microdiffraction domain if both the propagation distance z and the size of the integration area of Eq. (1) are comparable to λ.

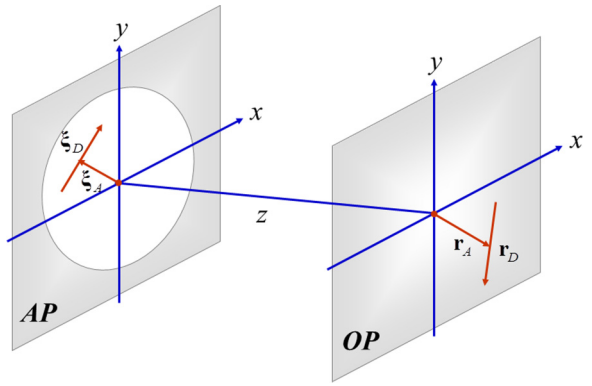

FIG. 1. (Color online) Geometry of the nonparaxial setups for the microdiffraction domain.

Now, conventional squared modulus detection is based on recording the local values of the electric power spectrum at the OP. Such values are theoretically predicted by evaluating Eq. (1) for $\mathbf{r}_D = 0$ [2], i.e.,

$$\mathbf{W}(\mathbf{r}_A,\mathbf{r}_A) = \int_{AP} d^2\xi_A\, \mathbf{W}(\boldsymbol{\xi}_A;\mathbf{r}_A;\lambda,z), \tag{3}$$

with

$$\mathbf{W}(\boldsymbol{\xi}_A;\mathbf{r}_A;\lambda,z) = \int_{AP} d^2\xi_D \;\; \boldsymbol{\Psi}(\boldsymbol{\xi}_+)\, \boldsymbol{\eta}(\boldsymbol{\xi}_+,\boldsymbol{\xi}_-)\, \boldsymbol{\Psi}(\boldsymbol{\xi}_-)$$
$$\times \langle |E_0(\boldsymbol{\xi}_+)|^2\rangle^{\frac{1}{2}}\, \langle |E_0(\boldsymbol{\xi}_-)|^2\rangle^{\frac{1}{2}}$$
$$\times \Phi(\boldsymbol{\xi}_+,\boldsymbol{\xi}_-;\mathbf{r}_A;\lambda,z), \tag{4a}$$

and

$$\Phi(\boldsymbol{\xi}_+,\boldsymbol{\xi}_-;\mathbf{r}_A;\lambda,z)$$
$$= \left(\frac{k}{4\pi}\right)^2 t(\boldsymbol{\xi}_+)\, t^*(\boldsymbol{\xi}_-) \left(\frac{z+|\mathbf{z}+\mathbf{r}_A-\boldsymbol{\xi}_A-\boldsymbol{\xi}_D/2|}{|\mathbf{z}+\mathbf{r}_A-\boldsymbol{\xi}_A-\boldsymbol{\xi}_D/2|^2}\right)$$
$$\times \left(\frac{z+|\mathbf{z}+\mathbf{r}_A-\boldsymbol{\xi}_A+\boldsymbol{\xi}_D/2\,|}{|\mathbf{z}+\mathbf{r}_A-\boldsymbol{\xi}_A+\boldsymbol{\xi}_D/2|^2}\right) \exp(i\,k\,|\mathbf{z}+\mathbf{r}_A-\boldsymbol{\xi}_A$$
$$-\boldsymbol{\xi}_D/2| - i\,k\,|\mathbf{z}+\mathbf{r}_A-\boldsymbol{\xi}_A+\boldsymbol{\xi}_D/2|). \tag{4b}$$

The modal expansion in Eq. (4a) gives the power contributed by all the correlated pairs of radiant point sources within the structured support of spatial coherence [6] centered at any $\boldsymbol{\xi}_A$. It includes the individual radiant point source at this point ($\boldsymbol{\xi}_D = 0$), if any. Such power is addressed at the support center $\boldsymbol{\xi}_A$ and distributed over the points $\mathbf{r}_A$ by the nonparaxial modes in Eq. (4b). Thus the electric power spectrum at the OP is obtained by simply adding the values of $\mathbf{W}(\boldsymbol{\xi}_A;\mathbf{r}_A;\lambda,z)$, as shown in Eq. (3).

Equation (4a) can be accurately calculated by modeling the planar source at the AP in terms of separated but inserted sets of radiant and virtual point sources [3], as conceptually sketched in Fig. 2.

The contributions of the sets of point sources can be separated by inserting the dimensionless function $1 \equiv \delta(\boldsymbol{\xi}_D) + [1-\delta(\boldsymbol{\xi}_D)]$ in the integral of Eq. (4a), with $\delta(\boldsymbol{\xi}_D)$ the Dirac δ (a unity constant with inverse units to the Dirac δ is implicitly

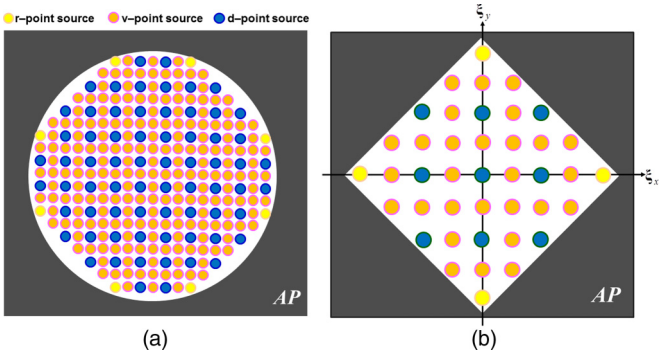

FIG. 2. (Color online) Conceptual sketches of the planar source modeling in terms of pure radiant (r), pure virtual (v), and dual (d) point sources. (a) Circular-shaped and (b) square-shaped planar sources. The Cartesian axes in (b) determine the ξ_A positions of the point sources.

assumed as the δ coefficient). It yields

$$\mathbf{W}(\boldsymbol{\xi}_A;\mathbf{r}_A;\lambda,z) = \mathbf{W}_{\rm rad}(\boldsymbol{\xi}_A;\mathbf{r}_A;\lambda,z) + \mathbf{W}_{\rm vir}(\boldsymbol{\xi}_A;\mathbf{r}_A;\lambda,z), \tag{5a}$$

with

$$\mathbf{W}_{\rm rad}(\boldsymbol{\xi}_A;\mathbf{r}_A;\lambda,z) = \boldsymbol{\Psi}(\boldsymbol{\xi}_A)\,\boldsymbol{\eta}(\boldsymbol{\xi}_A,\boldsymbol{\xi}_A)\,\boldsymbol{\Psi}(\boldsymbol{\xi}_A) \times \langle|E_0(\boldsymbol{\xi}_A)|^2\rangle\Phi(\boldsymbol{\xi}_A;\mathbf{r}_A;\lambda,z), \tag{5b}$$

obtained by evaluating Eq. (4a) for $\boldsymbol{\xi}_D = 0$, and $\mathbf{W}_{\rm vir}(\boldsymbol{\xi}_A;\mathbf{r}_A;\lambda,z)$ with the same form as Eq. (4a), under the condition $\boldsymbol{\xi}_D \neq 0$. Equation (5a) refers to the point source placed at a specific $\boldsymbol{\xi}_A$, which is pure radiant if $\mathbf{W}_{\rm vir}(\boldsymbol{\xi}_A;\mathbf{r}_A;\lambda,z) = 0$, pure virtual if $\mathbf{W}_{\rm rad}(\boldsymbol{\xi}_A;\mathbf{r}_A;\lambda,z) = 0$, and dual if both terms of Eq. (5a) take on non-null values. Equation (5b) points out that the emissions of all the radiant point sources are only transported by real valued and positive definite nonparaxial modes, with identical mathematical form given by

$$\Phi(\boldsymbol{\xi}_A;\mathbf{r}_A;\lambda,z) = \left(\frac{k}{4\pi}\right)^2 |t(\boldsymbol{\xi}_A)|^2 \left(\frac{z+|\mathbf{z}+\mathbf{r}_A-\boldsymbol{\xi}_A|}{|\mathbf{z}+\mathbf{r}_A-\boldsymbol{\xi}_A|^2}\right)^2. \tag{6}$$

In contrast, the emissions of the virtual point sources are transported by the modal expansion in Eq. (4a), which excludes the radiant modes in Eq. (6).

The requirement of pure virtual point sources implies the discreteness of the set of radiant point sources, although the complete arrangement of the radiant and the virtual sets can be a continuous distribution [7,8]. Even if the planar source is fully incoherent, empty places between consecutive radiant point sources must be taken into account in order to allocate the pure virtual point sources, turned on as the wave field gains in spatial coherence along its propagation [9]. Therefore, most of the integrals in the mathematical formulation of this theory are realized as summations. This feature provides a novel physical explanation of the mathematical properties of the generalized radiant emittance [10], for instance.

The modal expansion in Eq. (4a) is the key expression of the theory. It accounts for the transport of the emissions provided by the individual radiant, virtual, and dual point sources of the planar source, as defined by Eq. (5a). This treatment clearly differs from the conventional development of the second-order theory of spatial coherence [2,11]. An additional step is to expand the tensor integrand of Eq. (4a) in terms of the Pauli spin matrices [2]:

$$\boldsymbol{\sigma}_0 = \begin{bmatrix}1 & 0\\ 0 & 1\end{bmatrix}, \quad \boldsymbol{\sigma}_1 = \begin{bmatrix}1 & 0\\ 0 & -1\end{bmatrix},$$
$$\boldsymbol{\sigma}_2 = \begin{bmatrix}0 & 1\\ 1 & 0\end{bmatrix}, \quad \text{and } \boldsymbol{\sigma}_3 = \begin{bmatrix}0 & i\\ -i & 0\end{bmatrix},$$

with $i = \sqrt{-1}$, that is,

$$\boldsymbol{\Psi}(\boldsymbol{\xi}_+)\,\boldsymbol{\eta}(\boldsymbol{\xi}_+,\boldsymbol{\xi}_-)\,\boldsymbol{\Psi}(\boldsymbol{\xi}_-) = \frac{1}{2}\,\eta_0(\boldsymbol{\xi}_+,\boldsymbol{\xi}_-)\sum_{j=0}^{3}\mathbf{s}_j(\boldsymbol{\xi}_+,\boldsymbol{\xi}_-)\,\boldsymbol{\sigma}_j, \tag{7}$$

with the coefficients

$$\mathbf{s}_0(\boldsymbol{\xi}_+,\boldsymbol{\xi}_-) = \langle\cos\vartheta(\boldsymbol{\xi}_+)\cos\vartheta(\boldsymbol{\xi}_-)\rangle\,\langle\exp[i\,\beta_0(\boldsymbol{\xi}_+,\boldsymbol{\xi}_-)]\rangle + \langle\sin\vartheta(\boldsymbol{\xi}_+)\sin\vartheta(\boldsymbol{\xi}_-)\rangle\,\langle\exp[i\,\beta_0(\boldsymbol{\xi}_+,\boldsymbol{\xi}_-)]\rangle, \tag{8a}$$

$$\mathbf{s}_1(\boldsymbol{\xi}_+,\boldsymbol{\xi}_-) = \langle\cos\vartheta(\boldsymbol{\xi}_+)\cos\vartheta(\boldsymbol{\xi}_-)\rangle\,\langle\exp[i\,\beta_0(\boldsymbol{\xi}_+,\boldsymbol{\xi}_-)]\rangle - \langle\sin\vartheta(\boldsymbol{\xi}_+)\sin\vartheta(\boldsymbol{\xi}_-)\rangle\,\langle\exp[i\,\beta_0(\boldsymbol{\xi}_+,\boldsymbol{\xi}_-)]\rangle, \tag{8b}$$

$$\mathbf{s}_2(\boldsymbol{\xi}_+,\boldsymbol{\xi}_-) = \langle\cos\vartheta(\boldsymbol{\xi}_+)\sin\vartheta(\boldsymbol{\xi}_-)\rangle\,\langle\exp[i\,\beta_{xy}(\boldsymbol{\xi}_+,\boldsymbol{\xi}_-)\,]\rangle + \langle\sin\vartheta(\boldsymbol{\xi}_+)\cos\vartheta(\boldsymbol{\xi}_-)\rangle\,\langle\exp[i\,\beta_{yx}(\boldsymbol{\xi}_+,\boldsymbol{\xi}_-)]\rangle, \tag{8c}$$

$$\mathbf{s}_3(\boldsymbol{\xi}_+,\boldsymbol{\xi}_-) = -i\,\langle\cos\vartheta(\boldsymbol{\xi}_+)\sin\vartheta(\boldsymbol{\xi}_-)\rangle\,\langle\exp[i\,\beta_{xy}(\boldsymbol{\xi}_+,\boldsymbol{\xi}_-)]\rangle + i\,\langle\sin\vartheta(\boldsymbol{\xi}_+)\cos\vartheta(\boldsymbol{\xi}_-)\rangle\,\langle\exp[i\,\beta_{yx}(\boldsymbol{\xi}_+,\boldsymbol{\xi}_-)]\rangle, \tag{8d}$$

where $\beta_0(\boldsymbol{\xi}_+,\boldsymbol{\xi}_-) = \beta_{xx}(\boldsymbol{\xi}_+,\boldsymbol{\xi}_-) = \beta_{yy}(\boldsymbol{\xi}_+,\boldsymbol{\xi}_-)$ holds [3]. The expansion coefficients are generalized parameters that characterize the polarization state of electromagnetic wave fields in any state of spatial coherence [3]. They yield the (normalized) parameters introduced by Sir George Gabriel Stokes in 1852 [5,12] under the conditions $\boldsymbol{\xi}_D = 0$ and $\beta_{xy}(\boldsymbol{\xi}_A,\boldsymbol{\xi}_A) = -\beta_{yx}(\boldsymbol{\xi}_A,\boldsymbol{\xi}_A)$. In this sense, the Stokes parameters only determine the (local) polarization of the electric field vectors emitted by the radiant point sources. In contrast, the generalized parameters take into account an extended property in order to determine the polarization state of the field, i.e., the spatial correlation of the polarization functions defined in the Appendix, over the structured support centered at each $\boldsymbol{\xi}_A$. Consequently, the generalized parameters account for both the polarization of the radiant emissions and the polarization of the emissions of the virtual point sources. They are novel attributes conferred to the electromagnetic wave fields within the framework of the current unified theory of spatial coherence and polarization.

The physical meanings of the generalized parameters are the same as those of the corresponding Stokes parameters, i.e., they concern, respectively, the electric field power [Eq. (8a)], the linear polarizations along the x or y axes [Eq. (8b)], the

linear polarizations at $\pm\pi/4$ [Eq. (8c)], and the right and the left circular polarizations [Eq. (8d)].

Equations (4a) and (7) yield

$$\mathbf{W}(\boldsymbol{\xi}_A;\mathbf{r}_A;\lambda,z) = \begin{bmatrix} \boldsymbol{\kappa}_0(\boldsymbol{\xi}_A,\mathbf{r}_A)+\boldsymbol{\kappa}_1(\boldsymbol{\xi}_A,\mathbf{r}_A) & \boldsymbol{\kappa}_2(\boldsymbol{\xi}_A,\mathbf{r}_A)+i\,\boldsymbol{\kappa}_3(\boldsymbol{\xi}_A,\mathbf{r}_A) \\ \boldsymbol{\kappa}_2(\boldsymbol{\xi}_A,\mathbf{r}_A)-i\,\boldsymbol{\kappa}_3(\boldsymbol{\xi}_A,\mathbf{r}_A) & \boldsymbol{\kappa}_0(\boldsymbol{\xi}_A,\mathbf{r}_A)-\boldsymbol{\kappa}_1(\boldsymbol{\xi}_A,\mathbf{r}_A) \end{bmatrix} \tag{9a}$$

with

$$\boldsymbol{\kappa}_j(\boldsymbol{\xi}_A,\mathbf{r}_A) = \frac{1}{2}\int_{AP} d^2\xi_D \;\; \eta_0(\boldsymbol{\xi}_+,\boldsymbol{\xi}_-) \;\; \mathbf{s}_j(\boldsymbol{\xi}_+,\boldsymbol{\xi}_-) \times \langle |E_0(\boldsymbol{\xi}_+)|^2\rangle^{\frac{1}{2}} \;\langle |E_0(\boldsymbol{\xi}_-)|^2\rangle^{\frac{1}{2}} \times \Phi(\boldsymbol{\xi}_+,\boldsymbol{\xi}_-;\mathbf{r}_A;\lambda,z). \tag{9b}$$

Equations (9a) and (9b) allow factoring the integrand of Eq. (4a) in terms of the physical attributes of the electromagnetic wave field at the AP in such a way that:

$\boldsymbol{\kappa}_0(\boldsymbol{\xi}_A,\mathbf{r}_A)$ refers to the transport of the electric power depending on the spatial coherence at the AP given by $\eta_0(\boldsymbol{\xi}_+,\boldsymbol{\xi}_-)$, but with independence from the polarization state.

$\boldsymbol{\kappa}_{j>0}(\boldsymbol{\xi}_A,\mathbf{r}_A)$ refers to the transport of the power amount at the AP, associated to the states of polarization and spatial coherence determined by $\mathbf{s}_{j>0}(\boldsymbol{\xi}_+,\boldsymbol{\xi}_-)$ and $\eta_0(\boldsymbol{\xi}_+,\boldsymbol{\xi}_-)$ respectively.

After inserting the function $1 \equiv \delta(\boldsymbol{\xi}_D) + [1-\delta(\boldsymbol{\xi}_D)]$ in the integrand of $\mathbf{S}(\boldsymbol{\xi}_A,\mathbf{r}_A) = \mathrm{Tr}[\mathbf{W}(\boldsymbol{\xi}_A,\mathbf{r}_A)]$, follows

$$\mathbf{S}(\boldsymbol{\xi}_A,\mathbf{r}_A) = \mathbf{S}_{\mathrm{rad}}(\boldsymbol{\xi}_A,\mathbf{r}_A) + \mathbf{S}_{\mathrm{vir}}(\boldsymbol{\xi}_A,\mathbf{r}_A) \tag{10a}$$

with

$$\mathbf{S}_{\mathrm{rad}}(\boldsymbol{\xi}_A,\mathbf{r}_A) = \langle\, |E_0(\boldsymbol{\xi}_A)|^2\rangle \;\Phi(\boldsymbol{\xi}_A;\mathbf{r}_A;\lambda,z) \tag{10b}$$

and

$$\mathbf{S}_{\mathrm{vir}}(\boldsymbol{\xi}_A,\mathbf{r}_A) = 2\int_{\substack{AP\\ \boldsymbol{\xi}_D\neq 0}} d^2\xi_D \;\; \eta_0(\boldsymbol{\xi}_+,\boldsymbol{\xi}_-)\;\mathbf{s}_0(\boldsymbol{\xi}_+,\boldsymbol{\xi}_-) \times \langle |E_0(\boldsymbol{\xi}_+)|^2\rangle^{\frac{1}{2}} \;\langle |E_0(\boldsymbol{\xi}_-)|^2\rangle^{\frac{1}{2}} \times \mathrm{Re}[\Phi(\boldsymbol{\xi}_+,\boldsymbol{\xi}_-;\mathbf{r}_A;\lambda,z)], \tag{10c}$$

where the scalar kernel

$$2\,\mathrm{Re}[\Phi(\boldsymbol{\xi}_+,\boldsymbol{\xi}_-;\mathbf{r}_A;\lambda,z)] = 2\left(\frac{k}{4\pi}\right)^2 |t(\boldsymbol{\xi}_+)||t(\boldsymbol{\xi}_-)| \left(\frac{z+|\mathbf{z}+\mathbf{r}_A-\boldsymbol{\xi}_A-\boldsymbol{\xi}_D/2|}{|\mathbf{z}+\mathbf{r}_A-\boldsymbol{\xi}_A-\boldsymbol{\xi}_D/2|^2}\right)\left(\frac{z+|\mathbf{z}+\mathbf{r}_A-\boldsymbol{\xi}_A+\boldsymbol{\xi}_D/2|}{|\mathbf{z}+\mathbf{r}_A-\boldsymbol{\xi}_A+\boldsymbol{\xi}_D/2|^2}\right) \times \cos[k|\mathbf{z}+\mathbf{r}_A-\boldsymbol{\xi}_A-\boldsymbol{\xi}_D/2| - k|\mathbf{z}+\mathbf{r}_A-\boldsymbol{\xi}_A+\boldsymbol{\xi}_D/2| + \Delta\varphi(\boldsymbol{\xi}_+,\boldsymbol{\xi}_-)], \tag{10d}$$

with $\Delta\varphi(\boldsymbol{\xi}_+,\boldsymbol{\xi}_-) = \varphi(\boldsymbol{\xi}_+) - \varphi(\boldsymbol{\xi}_-)$, results by associating the modes

$$\Phi(\boldsymbol{\xi}_+,\boldsymbol{\xi}_-;\mathbf{r}_A;\lambda,z) + \Phi(\boldsymbol{\xi}_-,\boldsymbol{\xi}_+;\mathbf{r}_A;\lambda,z) = 2\,\mathrm{Re}[\Phi(\boldsymbol{\xi}_+,\boldsymbol{\xi}_-;\mathbf{r}_A;\lambda,z)],$$

because they are Hermitian, i.e.,

$$\Phi(\boldsymbol{\xi}_+,\boldsymbol{\xi}_-;\mathbf{r}_A;\lambda,z) = \Phi^*(\boldsymbol{\xi}_-,\boldsymbol{\xi}_+;\mathbf{r}_A;\lambda,z).$$

Equation (10b) is real valued, positive definite, and independent from the states of spatial coherence and polarization. It determines the transport of the electric power emitted by each radiant point source at the AP to any point on the OP, by means of nonparaxial modes with the same shape given by Eq. (6).

The modal expansion in Eq. (10c) describes the transport of the modulating power, emitted by the virtual point source at $\boldsymbol{\xi}_A$, to any point $\mathbf{r}_A$, through the time-independent and deterministic space structure that oscillates between positive and negative values in accordance to the kernel [Eq. (10d)]. The expansion is real valued, too, and its coefficients are closely related to the states of spatial coherence and polarization, specified by the factors $\eta_0(\boldsymbol{\xi}_+,\boldsymbol{\xi}_-)\mathbf{s}_0(\boldsymbol{\xi}_+,\boldsymbol{\xi}_-)$.

The expansion modes can be ordered according to $|\boldsymbol{\xi}_D|$, so that the longer $|\boldsymbol{\xi}_D|$ the higher the mode order. Accordingly, Eq. (6) defines the 0-order modes, while high-order modes defined in Eq. (4b) determine the kernel in Eq. (10d) [4].

The physical features attributed to $\boldsymbol{\kappa}_j(\boldsymbol{\xi}_A,\mathbf{r}_A)$ lead to $\det[\mathbf{W}(\boldsymbol{\xi}_A,\mathbf{r}_A)] \geqslant 0$, and therefore

$$0 \leqslant \sqrt{\boldsymbol{\kappa}_1^2(\boldsymbol{\xi}_A,\mathbf{r}_A)+\boldsymbol{\kappa}_2^2(\boldsymbol{\xi}_A,\mathbf{r}_A)+\boldsymbol{\kappa}_3^2(\boldsymbol{\xi}_A,\mathbf{r}_A)} \leqslant \boldsymbol{\kappa}_0(\boldsymbol{\xi}_A,\mathbf{r}_A),$$

with $\sqrt{\boldsymbol{\kappa}_1^2(\boldsymbol{\xi}_A,\mathbf{r}_A)+\boldsymbol{\kappa}_2^2(\boldsymbol{\xi}_A,\mathbf{r}_A)+\boldsymbol{\kappa}_3^2(\boldsymbol{\xi}_A,\mathbf{r}_A)}$

the transport descriptor for the polarized component of the field. Thus the dimensionless quantity,

$$\mathbf{P}(\boldsymbol{\xi}_A,\mathbf{r}_A) = \sqrt{\frac{\boldsymbol{\kappa}_1^2(\boldsymbol{\xi}_A,\mathbf{r}_A)+\boldsymbol{\kappa}_2^2(\boldsymbol{\xi}_A,\mathbf{r}_A)+\boldsymbol{\kappa}_3^2(\boldsymbol{\xi}_A,\mathbf{r}_A)}{\boldsymbol{\kappa}_0^2(\boldsymbol{\xi}_A,\mathbf{r}_A)}} = \sqrt{1-\frac{4\;\det[W(\boldsymbol{\xi}_A,\mathbf{r}_A)]}{\mathrm{Tr}^2[W(\boldsymbol{\xi}_A,\mathbf{r}_A)]}} \tag{10e}$$

takes on positive definite values in the interval [0, 1] that involves contributions of both the radiant and the virtual point sources and denotes the degree of polarization of the electromagnetic wave field transported from $\boldsymbol{\xi}_A$ to $\mathbf{r}_A$. So, it is reasonable to call it the nonparaxial polarization parameter.

It is apparent that $\mathbf{P}(\boldsymbol{\xi}_A,\mathbf{r}_A) = 0$ holds if $\boldsymbol{\kappa}_{j>0}(\boldsymbol{\xi}_A,\mathbf{r}_A) = 0$ holds too, while $\mathbf{P}(\boldsymbol{\xi}_A,\mathbf{r}_A) = 1$ holds if $\boldsymbol{\kappa}_1^2(\boldsymbol{\xi}_A,\mathbf{r}_A)+\boldsymbol{\kappa}_2^2(\boldsymbol{\xi}_A,\mathbf{r}_A)+\boldsymbol{\kappa}_3^2(\boldsymbol{\xi}_A,\mathbf{r}_A) = \boldsymbol{\kappa}_0^2(\boldsymbol{\xi}_A,\mathbf{r}_A)$ stands. Thus, $\boldsymbol{\kappa}_{j_0}^2(\boldsymbol{\xi}_A,\mathbf{r}_A) = \boldsymbol{\kappa}_0^2(\boldsymbol{\xi}_A,\mathbf{r}_A)$ and $\boldsymbol{\kappa}_{j\neq j_0}(\boldsymbol{\xi}_A,\mathbf{r}_A) = 0$ stand for $j,\ j_0 > 0$, if $\boldsymbol{\kappa}_{j_0>0}(\boldsymbol{\xi}_A,\mathbf{r}_A)$ determines the polarization state of the field emitted by the point source at $\boldsymbol{\xi}_A$ and transported to $\mathbf{r}_A$.

According to the analysis above, the diagonal elements of the tensor in Eq. (9a) concern the transport of the radiant

and the modulating powers, as well as the linear polarization state along any of the Cartesian x or y axes, while its off-diagonal elements concern the $\pm\pi/4$ linear and the (right, left) circular polarization states. Furthermore, the insertion of $1 \equiv \delta(\boldsymbol{\xi}_D) + [1 - \delta(\boldsymbol{\xi}_D)]$ in the integral of Eq. (9b) yields $\boldsymbol{\kappa}_j(\boldsymbol{\xi}_A,\mathbf{r}_A) = \boldsymbol{\kappa}_j^{(\mathrm{rad})}(\boldsymbol{\xi}_A,\mathbf{r}_A) + \boldsymbol{\kappa}_j^{(\mathrm{vir})}(\boldsymbol{\xi}_A,\mathbf{r}_A)$, with

$$\boldsymbol{\kappa}_j^{(\mathrm{rad})}(\boldsymbol{\xi}_A,\mathbf{r}_A) = \tfrac{1}{2}\,\langle |E_0(\boldsymbol{\xi}_A)|^2\rangle\ \mathbf{s}_j(\boldsymbol{\xi}_A,\boldsymbol{\xi}_A)\Phi(\boldsymbol{\xi}_A;\mathbf{r}_A;\lambda,z) \tag{11a}$$

the radiant point source contribution, and

$$\begin{aligned}\boldsymbol{\kappa}_j^{(\mathrm{vir})}(\boldsymbol{\xi}_A,\mathbf{r}_A) = \int_{\substack{AP\\ \boldsymbol{\xi}_D\neq 0}} d^2\xi_D\ \ \eta_0(\boldsymbol{\xi}_+,\boldsymbol{\xi}_-)\ \langle\,|E_0(\boldsymbol{\xi}_+)\,|^2\rangle^{\frac{1}{2}}\\ \times\,\langle\,|E_0(\boldsymbol{\xi}_-)\,|^2\rangle^{\frac{1}{2}}\ s_j(\boldsymbol{\xi}_+,\boldsymbol{\xi}_-)\\ \times\,\mathrm{Re}\,[\,\Phi(\boldsymbol{\xi}_+,\boldsymbol{\xi}_-;\mathbf{r}_A;\lambda,z)\,]\end{aligned} \tag{11b}$$

the virtual point source contribution. As before, $\boldsymbol{\kappa}_j^{(\mathrm{vir})}(\boldsymbol{\xi}_A,\mathbf{r}_A) = 0$ holds for pure radiant point sources, $\boldsymbol{\kappa}_j^{(\mathrm{rad})}(\boldsymbol{\xi}_A,\mathbf{r}_A) = 0$ holds for pure virtual point sources, and both terms must be considered for dual point sources. In addition, $\mathbf{S}_{\mathrm{rad}}(\boldsymbol{\xi}_A,\mathbf{r}_A) = 2\,\boldsymbol{\kappa}_0^{(\mathrm{rad})}(\boldsymbol{\xi}_A,\mathbf{r}_A)$ and $\mathbf{S}_{\mathrm{vir}}(\boldsymbol{\xi}_A,\mathbf{r}_A) = 2\,\boldsymbol{\kappa}_0^{(\mathrm{vir})}(\boldsymbol{\xi}_A,\mathbf{r}_A)$ denote, respectively, the radiant and the modulating powers, emitted at $\boldsymbol{\xi}_A$ and transported to $\mathbf{r}_A$. It is remarkable that the nonparaxial 0-order modes defined in Eq. (6) are also associated to $\boldsymbol{\kappa}_j^{(\mathrm{rad})}(\boldsymbol{\xi}_A,\mathbf{r}_A)$, while the nonparaxial high-order modes defined in Eq. (10d) are associated to $\boldsymbol{\kappa}_j^{(\mathrm{vir})}(\boldsymbol{\xi}_A,\mathbf{r}_A)$.

Summarizing, the space structure determined by the scalar nonparaxial modes is independent from the emission events of both the radiant and the modulating powers, as well as from the choice of the Cartesian axes defined for the polarization state. Nevertheless, the 0-order modes only transport the physical attributes of the electromagnetic wave field due to the set of radiant point sources (i.e., the radiant power and the Stokes polarization states); while the expansion of high-order modes transports the physical attributes due to the set of virtual point sources (i.e., the modulating power and the states of spatial coherence and polarization characterized by the generalized parameters). Furthermore, the 0-order modes are quite different from the high-order modes. i.e., the former ones are positive definite with shape-invariant Lorentzian cross sections along the z axis, while the last ones have cosinelike oscillations with Lorentzian modulation in amplitude and spatial frequency chirping (due to the nonlinearity of the propagator argument), and their cross sections are not invariant along the z axis mainly in the microdiffraction domain [4].

The expression

$$\begin{aligned}&\int_{AP}\int_{OP}\mathbf{S}(\boldsymbol{\xi}_A,\mathbf{r}_A)\,d^2\xi_A\,d^2r_A\\ &=\int_{AP}\int_{OP}\mathbf{S}_{\mathrm{rad}}(\boldsymbol{\xi}_A,\mathbf{r}_A)\,d^2\xi_A\,d^2r_A\\ &\quad+\int_{AP}\int_{OP}\mathbf{S}_{\mathrm{vir}}(\boldsymbol{\xi}_A,\mathbf{r}_A)\,d^2\xi_A\,d^2r_A\end{aligned} \tag{12a}$$

epitomizes the conservation law of the total electric energy of the field over the planes of the setup transversal to the direction of propagation, with

$$\begin{aligned}&\int_{AP}\int_{OP}\mathbf{S}_{\mathrm{rad}}(\boldsymbol{\xi}_A,\mathbf{r}_A)\,d^2\xi_A\,d^2r_A\\ &=\int_{AP}\langle\,|E_0(\boldsymbol{\xi}_A)\,|^2\rangle\ \mathbf{s}_0(\boldsymbol{\xi}_A,\boldsymbol{\xi}_A)\\ &\quad\times\int_{OP}\Phi(\boldsymbol{\xi}_A;\mathbf{r}_A;\lambda,z)\,d^2r_A\,d^2\xi_A\end{aligned} \tag{12b}$$

the total radiant energy, and

$$\begin{aligned}&\int_{AP}\int_{OP}\mathbf{S}_{\mathrm{vir}}(\boldsymbol{\xi}_A,\mathbf{r}_A)\,d^2\xi_A\,d^2r_A\\ &=2\int_{AP}d^2\xi_A\int_{\substack{AP\\ \boldsymbol{\xi}_D\neq 0}}\eta_0(\boldsymbol{\xi}_+,\boldsymbol{\xi}_-)\,\langle\,|E_0(\boldsymbol{\xi}_+)\,|^2\rangle^{\frac{1}{2}}\\ &\quad\times\langle\,|E_0(\boldsymbol{\xi}_-)\,|^2\rangle^{\frac{1}{2}}\ \mathbf{s}_0(\boldsymbol{\xi}_+,\boldsymbol{\xi}_-)\\ &\quad\times\int_{OP}\mathrm{Re}\,[\,\Phi(\boldsymbol{\xi}_+,\boldsymbol{\xi}_-;\mathbf{r}_A;\lambda,z)\,]\,d^2r_A\,d^2\xi_D\end{aligned} \tag{12c}$$

the total modulating energy. Furthermore,

$$\begin{aligned}&\int_{AP}Tr[\boldsymbol{\Psi}(\boldsymbol{\xi}_A)\,\boldsymbol{\eta}(\boldsymbol{\xi}_A,\boldsymbol{\xi}_A)\,\boldsymbol{\Psi}(\boldsymbol{\xi}_A)\,]\,d^2\xi_A\\ &=\int_{AP}[\langle\,|E_x(\boldsymbol{\xi}_A)\,|^2\rangle\ +\ \langle\,|E_y(\boldsymbol{\xi}_A)\,|^2\rangle]\,d^2\xi_A\end{aligned} \tag{13}$$

represents the total electric energy emitted by the planar source at the AP. Therefore Eqs. (12a)–(12c) and (13) lead to the following conclusions:

(i) The nonparaxial 0-order modes must be normalized, i.e.,

$$\int_{OP}\Phi(\boldsymbol{\xi}_A;\mathbf{r}_A;\lambda,z)\,d^2r_A = 1. \tag{14a}$$

So, they must spread without changing their shapes because their maxima decay following the $1/z^2$ law [5].

(ii) The total modulating energy must nullify, i.e.,

$$\int_{AP}\int_{OP}\mathbf{S}_{\mathrm{vir}}(\boldsymbol{\xi}_A,\mathbf{r}_A)\,d^2\xi_A\,d^2r_A = 0, \tag{14b}$$

and therefore

$$\int_{OP}\mathrm{Re}[\Phi(\boldsymbol{\xi}_+,\boldsymbol{\xi}_-;\mathbf{r}_A;\lambda,z)\,]\,d^2r_A = 0.$$

This result confirms that the high-order nonparaxial modes must oscillate between positive and negative values.

Now, the electric power spectrum of the electromagnetic wave field at any point on the OP takes the form

$$S(\mathbf{r}_A) = \int_{AP}\mathbf{S}(\boldsymbol{\xi}_A,\mathbf{r}_A)\,d^2\xi_A = S_{\mathrm{rad}}(\mathbf{r}_A) + S_{\mathrm{vir}}(\mathbf{r}_A). \tag{15a}$$

It is real valued and positive definite, with

$$\begin{aligned}S_{\mathrm{rad}}(\mathbf{r}_A) &= \int_{AP}\mathbf{S}_{\mathrm{rad}}(\boldsymbol{\xi}_A,\mathbf{r}_A)\,d^2\boldsymbol{\xi}_A\\ &=\int_{AP}\langle|E_0(\boldsymbol{\xi}_A)|^2\rangle\mathbf{s}_0(\boldsymbol{\xi}_A,\boldsymbol{\xi}_A)\Phi(\boldsymbol{\xi}_A;\mathbf{r}_A;\lambda,z)\,d^2\xi_A\end{aligned} \tag{15b}$$

the positive definite total radiant power, and

$$S_{\rm vir}(\mathbf{r}_A) = \int_{AP} S_{\rm vir}(\boldsymbol{\xi}_A,\mathbf{r}_A)\, d^2\xi_A$$
$$= 2\int_{AP} d^2\xi_A \int_{\substack{AP\\ \boldsymbol{\xi}_D\neq 0}} d^2\xi_D \;\; \eta_0(\boldsymbol{\xi}_+,\boldsymbol{\xi}_-)$$
$$\times \langle |E_0(\boldsymbol{\xi}_+)|^2\rangle^{\frac{1}{2}}\, \langle |E_0(\boldsymbol{\xi}_-)|^2\rangle^{\frac{1}{2}}\, \mathbf{s}_0(\boldsymbol{\xi}_+,\boldsymbol{\xi}_-)$$
$$\times {\rm Re}[\Phi(\boldsymbol{\xi}_+,\boldsymbol{\xi}_-;\mathbf{r}_A;\lambda,z)] \qquad (15c)$$

the total modulating power, which oscillates between positive and negative values in spite of its energy units. Thus it follows $S_{\rm rad}(\mathbf{r}_A) \geqslant |\, S_{\rm vir}(\mathbf{r}_A)\,|$ for $S_{\rm vir}(\mathbf{r}_A) \leqslant 0$. Therefore the addition of the total modulating power to the total radiant power is a redistribution mechanism of the last one, according to the shape of the space structure in the setup, and without disturbing the conservation law of the total energy.

III. ILLUSTRATIVE EXAMPLES

A. Natural light

This type of electromagnetic wave fields is nonpolarized, because their polarization angles randomly fluctuate in the interval $[-\pi,\pi]$, so that

$$\langle \cos\vartheta(\boldsymbol{\xi}_\pm)\rangle = \langle \sin\vartheta(\boldsymbol{\xi}_\pm)\rangle = 0 \text{ and } \langle \cos\vartheta(\boldsymbol{\xi}_\pm)\,\sin\vartheta(\boldsymbol{\xi}_\mp)\rangle = 0$$

and/or

$$\langle \exp[i\,\beta_{xy}(\boldsymbol{\xi}_+,\boldsymbol{\xi}_-)\,]\rangle = \langle \exp[i\,\beta_{yx}(\boldsymbol{\xi}_+,\boldsymbol{\xi}_-)\,]\rangle = 0$$

stand. Consequently, $\mathbf{s}_{j>1}(\boldsymbol{\xi}_+,\boldsymbol{\xi}_-) = 0$ and $\boldsymbol{\kappa}_{j>1}(\boldsymbol{\xi}_A,\mathbf{r}_A) = 0$ stand, too. Nevertheless, the random fluctuations of the polarization angles include coincidences in orientation of the electric field vectors at $\boldsymbol{\xi}_\pm$, for which $\langle \cos\vartheta(\boldsymbol{\xi}_+)\,\cos\vartheta(\boldsymbol{\xi}_-)\rangle = \langle \sin\vartheta(\boldsymbol{\xi}_+)\,\sin\vartheta(\boldsymbol{\xi}_-)\rangle = 1/2$ holds. Accordingly, $\mathbf{s}_0(\boldsymbol{\xi}_+,\boldsymbol{\xi}_-) = \langle \exp[i\,\beta_0(\boldsymbol{\xi}_+,\boldsymbol{\xi}_-)\,]\rangle$ and $\mathbf{s}_1(\boldsymbol{\xi}_+,\boldsymbol{\xi}_-) = 0$ stand, and then $\mathbf{P}(\boldsymbol{\xi}_A,\mathbf{r}_A) = 0$. In addition,

$$\mathbf{W}_{xx}(\boldsymbol{\xi}_A;\mathbf{r}_A;\lambda,z) = \mathbf{W}_{yy}(\boldsymbol{\xi}_A;\mathbf{r}_A;\lambda,z) = \boldsymbol{\kappa}_0(\boldsymbol{\xi}_A,\mathbf{r}_A) \qquad (16a)$$

defines the average (radiant and/or modulating) electric powers per Cartesian component of the electric field vectors emitted by the (radiant and/or virtual) point source at $\boldsymbol{\xi}_A$ and transported to $\mathbf{r}_A$, with

$$\boldsymbol{\kappa}_0(\boldsymbol{\xi}_A,\mathbf{r}_A) = \frac{1}{2}\langle |E_0(\boldsymbol{\xi}_A)|^2\rangle\; \Phi(\boldsymbol{\xi}_A;\mathbf{r}_A;\lambda,z)$$
$$+\frac{1}{2}\int_{\substack{AP\\ \boldsymbol{\xi}_D\neq 0}} d^2\xi_D \;\; \eta_0(\boldsymbol{\xi}_+,\boldsymbol{\xi}_-)\langle \exp[i\,\beta_0(\boldsymbol{\xi}_+,\boldsymbol{\xi}_-)]\rangle$$
$$\times \langle |E_0(\boldsymbol{\xi}_+)|^2\rangle^{\frac{1}{2}}\langle |E_0(\boldsymbol{\xi}_-)|^2\rangle^{\frac{1}{2}}\Phi(\boldsymbol{\xi}_+,\boldsymbol{\xi}_-;\mathbf{r}_A;\lambda,z). \qquad (16b)$$

Because of the attributes above, natural light is a scalar wave field, whose power spectrum at the OP in the microdiffraction domain becomes

$$S(\mathbf{r}_A)$$
$$= \int_{AP} \langle |E_0(\boldsymbol{\xi}_A)|^2\rangle\; \Phi(\boldsymbol{\xi}_A;\mathbf{r}_A;\lambda,z)\, d^2\xi_A$$
$$+ 2\int_{AP} d^2\xi_A \int_{\substack{AP\\ \boldsymbol{\xi}_D\neq 0}} d^2\xi_D\, \langle |E_0(\boldsymbol{\xi}_+)|^2\rangle^{\frac{1}{2}}\langle |E_0(\boldsymbol{\xi}_-)|^2\rangle^{\frac{1}{2}}$$
$$\times \eta_0(\boldsymbol{\xi}_+,\boldsymbol{\xi}_-)\,{\rm Re}\{\Phi(\boldsymbol{\xi}_+,\boldsymbol{\xi}_-;\mathbf{r}_A;\lambda,z)\langle \exp[i\,\beta_0(\boldsymbol{\xi}_+,\boldsymbol{\xi}_-)]\rangle\}\,. \qquad (17)$$

The quantity $\mu(\boldsymbol{\xi}_+,\boldsymbol{\xi}_-) = \eta_0(\boldsymbol{\xi}_+,\boldsymbol{\xi}_-)\,\langle \exp[i\,\beta_0(\boldsymbol{\xi}_+,\boldsymbol{\xi}_-)\,]\rangle$ involved in the integrand of the total modulating power in Eq. (17) is the complex degree of spatial coherence for scalar wave fields at the AP [2,5]. Amplitude uncorrelated electric field vectors and/or random phase differences in the interval $[-\pi,\pi]$ nullify $\mu(\boldsymbol{\xi}_+,\boldsymbol{\xi}_-)$ and make natural light spatially incoherent. However, natural light can contain relative small structured supports of spatial coherence, within which the correlation of the electric field vectors is significant and the phase difference $\beta_0(\boldsymbol{\xi}_+,\boldsymbol{\xi}_-)$ is quasideterministic. For this reason, Thomas Young could perform its celebrated interference experiment in 1801 [5].

Figures 3 and 4 illustrate the transport of the total radiant power and the total modulating power in the microdiffraction domain, respectively. A planar source of natural light is considered, composed by a line of three identical radiant point sources with spacing 5λ ($\lambda = 0.632\,\mu$m). The graphs (a) and (b) of both figures reveal the time-independent and deterministic space structure imposed by the 0-order nonparaxial modes (Fig. 3) and by the expansion of three high-order modes under the conditions $\Delta\varphi(\boldsymbol{\xi}_+,\boldsymbol{\xi}_-) = 0$ and $\beta_0(\boldsymbol{\xi}_+,\boldsymbol{\xi}_-) = 0$ (Fig. 4), respectively. The expansion contains two first-order modes for the powers $\mathbf{S}_{\rm vir}(\pm 2.5\lambda,\mathbf{r}_A)$, emitted by the virtual point sources corresponding to $\boldsymbol{\xi}_D = 5\lambda$, and one second-order

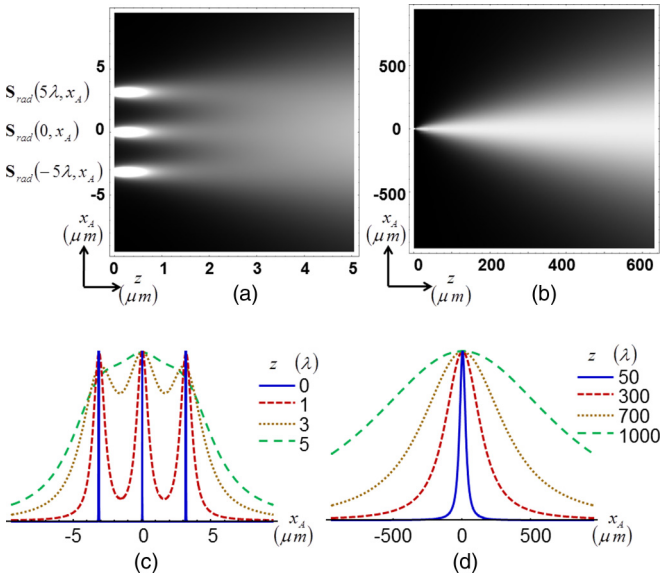

FIG. 3. (Color online) Transport of the power emitted by three radiant point sources at the scale metric $\lambda = 0.632\ \mu$m in the microdiffraction domain. Zero-order nonparaxial modes for (a) $0 \leqslant z \leqslant 8\lambda$ and (b) $0 \leqslant z \leqslant 10^3\lambda$. (c, d) Cross-section profiles at specific propagation distances in (a) and (b), respectively. The contributions of the individual radiant point sources are resolved in (a) and (c), but not in (b) and (d). The modes are enhanced and the profiles are scaled for presentation purposes.

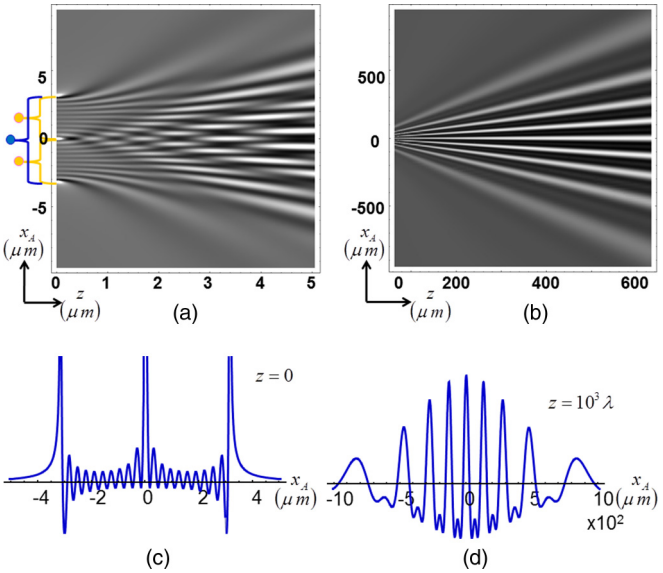

FIG. 4. (Color online) Modal expansion for the transport of the modulating power emitted by the three virtual point sources associated to the radiant point sources in Fig. 3, at the scale metric $\lambda = 0.632\ \mu$m, for (a) $0 \leqslant z \leqslant 8\lambda$ and (b) $10^2\lambda \leqslant z \leqslant 10^3\lambda$. (c, d) Cross-section profiles at specific propagation distances in (a) and (b), respectively. The positions of the virtual point sources are represented by the small circles in (a), and the corresponding pairs of radiant point sources is indicated. The modal expansion is enhanced and the main maxima in (c) are truncated for presentation purposes.

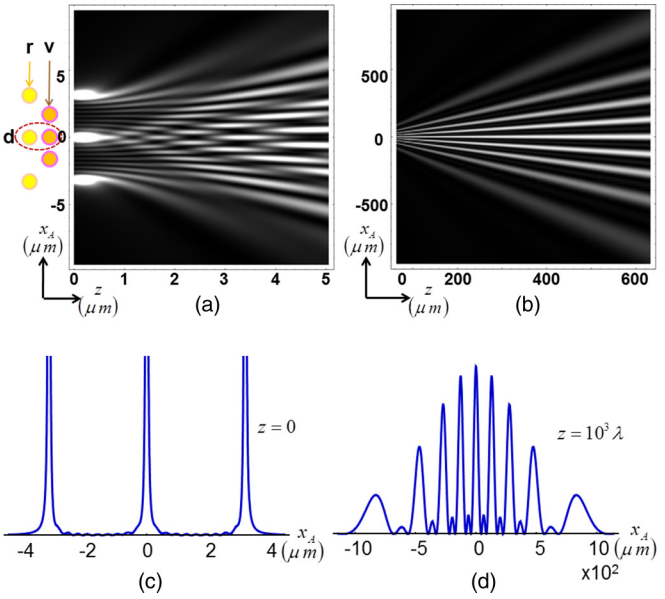

FIG. 5. (Color online) Transport of the power spectrum provided by the strong correlated radiant point sources in Fig. 3 along (a) $0 \leqslant z \leqslant 8\lambda$ and (b) $10^2\lambda \leqslant z \leqslant 10^3\lambda$. (c, d) Power spectra profiles, corresponding to the cross sections of (a) and (b) at specific propagation distances. The positions of the radiant r and the virtual v point sources are represented by the small circles in (a). The graphs in (a) and (b) are enhanced and the main maxima in (c) are truncated for presentation purposes.

mode for the power $\mathbf{S}_{\text{vir}}(0,\mathbf{r}_A)$, emitted by the virtual point source corresponding to $\boldsymbol{\xi}_D = 10\lambda$.

It is apparent that the radiant power flows through cones with vertex on the corresponding radiant point sources, which encloses more than the 90% of the electric power within an aperture of about 70°. Their superposition gives a resulting cone with similar characteristics as the individual ones. It is worth noting that these cones determine the only structure involved in the transport of spatially incoherent electromagnetic wave fields.

The transport of the modulating power of spatially partially coherent fields is performed through the fringe structure in Fig. 4, in accordance to the values of $\eta_0(\boldsymbol{\xi}_+,\boldsymbol{\xi}_-)$. It means that the higher $\eta_0(\boldsymbol{\xi}_+,\boldsymbol{\xi}_-)$ the greater the amount of transported modulating power, in such a way that the maximum amount is transported by fully spatial coherence, i.e., by $\eta_0(\boldsymbol{\xi}_+,\boldsymbol{\xi}_-) = 1$. The profiles for $z = 0$ in Figs. 3(c) and 4(c), respectively, reproduce the distribution of the radiant point sources at the AP and the spatial links between them, due to the correlations of their emissions. This physical meaning is not reported in the conventional second-order theory of electromagnetic spatial coherence [2].

Figure 5 illustrates the transport of the power spectrum in the microdiffraction domain, by assuming the planar source of natural light in Fig. 3 as fully spatially coherent, i.e., as composed by two pure radiant point sources (r) at $\boldsymbol{\xi}_A = \pm 5\lambda$, two pure virtual point sources (v) at $\boldsymbol{\xi}_A = \pm 2.5\lambda$, and one dual point source (d) at $\boldsymbol{\xi}_A = 0$. The main peaks of the profile (c) reproduce the radiant point source distribution at the AP, and their small spreading (note that they are truncated) is due to the Lorentzian cross section of the nonparaxial modes even by $z = 0$. In addition, the correlations between the radiant point sources cause very weak oscillations between the main peaks.

The interference pattern in (d) exhibits highly contrasted main maxima with secondary weak maxima in between, as expected for three spatially coherent radiant point sources. The Lorentzian envelope modulates the power distribution, and the spatial frequency chirping determines the fringe distribution. Graphs and profiles in Fig. 5 show the significant changes of the power spectrum distribution over the planes of the setup transversal to the direction of propagation in the microdiffraction domain. Such behavior is not predicted by the conventional formulation of the second-order theory of spatial coherence [2].

If the correlations between the radiant point sources diminish, the contrast of the fringe pattern diminishes too. In addition, the transversal shifts of the mode oscillations given by non-null phase differences $\Delta\varphi(\boldsymbol{\xi}_+,\boldsymbol{\xi}_-)$ and $\beta_0(\boldsymbol{\xi}_+,\boldsymbol{\xi}_-)$ change the fringe structure of the space. These features change the redistribution scheme for the radiant power, as shown in Fig. 6 for the same planar source in Fig. 3 with $\eta_0(5\lambda) = 0.778\,801$ and $\beta_0(5\lambda) = \pi/2$, $\eta_0(10\lambda) = 0.367\,879$, and $\beta_0(10\lambda) = \pi$.

The analysis above can also be applied to sources of nonpolarized wave fields different from natural light, such as nonpolarized lasers and LEDs.

B. Linearly polarized light parallel to the *x* axis

Electromagnetic wave fields whose polarization angles have narrow fluctuations around $\vartheta(\boldsymbol{\xi}_\pm) = 0$ are linear polarized along the Cartesian x axis. In this case

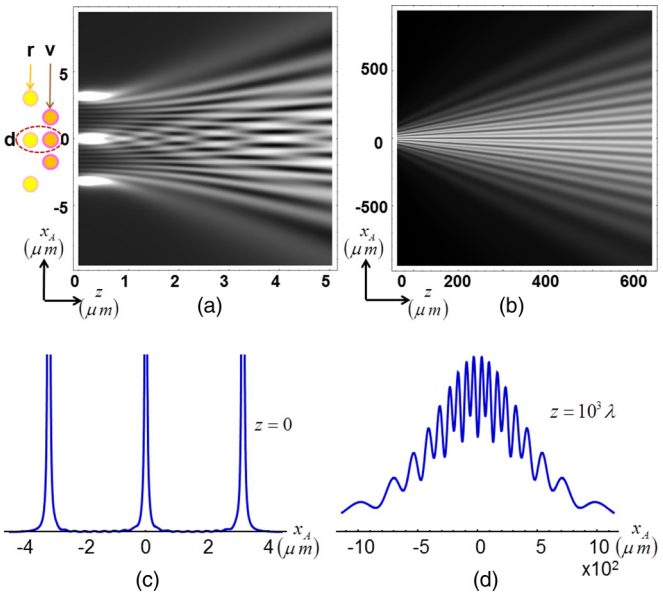

FIG. 6. (Color online) Transport of the power spectrum emitted by the partially correlated radiant point sources in Fig. 3 for (a) $0 \leqslant z \leqslant 8\lambda$ and (b) $10^2\lambda \leqslant z \leqslant 10^3\lambda$. (c, d) Power spectra profiles corresponding to the cross sections of (a) and (b) at specific propagation distances. The positions of the radiant r and the virtual v point sources are represented by the small circles in (a). The graphs in (a) and (b) are enhanced and the main maxima in (c) are truncated for presentation purposes.

$\langle \cos\vartheta(\boldsymbol{\xi}_\pm)\rangle = 1$, $\langle \sin\vartheta(\boldsymbol{\xi}_\pm)\rangle = 0$, $\langle \cos\vartheta(\boldsymbol{\xi}_+)\cos\vartheta(\boldsymbol{\xi}_-)\rangle = 1$, $\langle \sin\vartheta(\boldsymbol{\xi}_+)\sin\vartheta(\boldsymbol{\xi}_-)\rangle = 0$ hold. Thus, $\mathbf{s}_0(\boldsymbol{\xi}_+,\boldsymbol{\xi}_-) = \mathbf{s}_1(\boldsymbol{\xi}_+,\boldsymbol{\xi}_-) = \langle \exp[i\,\beta_0(\boldsymbol{\xi}_+,\boldsymbol{\xi}_-)]\rangle$ and $\langle \cos\vartheta(\boldsymbol{\xi}_\pm)\,\sin\vartheta(\boldsymbol{\xi}_\mp)\rangle = 0$ stand, so that $\mathbf{s}_2(\boldsymbol{\xi}_+,\boldsymbol{\xi}_-) = \mathbf{s}_3(\boldsymbol{\xi}_+,\boldsymbol{\xi}_-) = 0$. Therefore Eq. (9b) yields $\boldsymbol{\kappa}_2(\boldsymbol{\xi}_A,\mathbf{r}_A) = \boldsymbol{\kappa}_3(\boldsymbol{\xi}_A,\mathbf{r}_A) = 0$, and

$$\begin{aligned}\boldsymbol{\kappa}_0(\boldsymbol{\xi}_A,\mathbf{r}_A) &= \boldsymbol{\kappa}_1(\boldsymbol{\xi}_A,\mathbf{r}_A)\\ &= \frac{1}{2}\langle |E_0(\boldsymbol{\xi}_A)|^2\rangle\ \Phi(\boldsymbol{\xi}_A;\mathbf{r}_A;\lambda,z)\\ &\quad + \frac{1}{2}\int_{\substack{AP\\ \boldsymbol{\xi}_D\neq 0}} d^2\xi_D\ \eta_0(\boldsymbol{\xi}_+,\boldsymbol{\xi}_-)\langle \exp[i\,\beta_0(\boldsymbol{\xi}_+,\boldsymbol{\xi}_-)]\rangle\\ &\quad \times \langle |E_0(\boldsymbol{\xi}_+)|^2\rangle^{\frac{1}{2}}\langle |E_0(\boldsymbol{\xi}_-)|^2\rangle^{\frac{1}{2}}\Phi(\boldsymbol{\xi}_+,\boldsymbol{\xi}_-;\mathbf{r}_A;\lambda,z).\end{aligned} \tag{18}$$

The mathematical form and the physical meaning of Eq. (18) are equal to those of Eq. (16), but the condition $\boldsymbol{\kappa}_0(\boldsymbol{\xi}_A,\mathbf{r}_A) = \boldsymbol{\kappa}_1(\boldsymbol{\xi}_A,\mathbf{r}_A)$ states that the average electric (radiant and/or modulating) power, transported from $\boldsymbol{\xi}_A$ to $\mathbf{r}_A$, is linearly polarized parallel to the x axis, so that $\mathbf{P}(\boldsymbol{\xi}_A,\mathbf{r}_A) = 1$. It thus follows that

$$\mathbf{W}_{xx}(\boldsymbol{\xi}_A;\mathbf{r}_A;\lambda,z) = \boldsymbol{\kappa}_0(\boldsymbol{\xi}_A,\mathbf{r}_A) + \boldsymbol{\kappa}_1(\boldsymbol{\xi}_A,\mathbf{r}_A) \tag{19a}$$

and

$$\begin{aligned}&\mathbf{W}_{xy}(\boldsymbol{\xi}_A;\mathbf{r}_A;\lambda,z)\\ &\quad = \mathbf{W}_{yx}(\boldsymbol{\xi}_A;\mathbf{r}_A;\lambda,z) = \mathbf{W}_{yy}(\boldsymbol{\xi}_A;\mathbf{r}_A;\lambda,z) = 0.\end{aligned} \tag{19b}$$

Consequently, the power spectrum at the OP in the microdiffraction domain becomes the same mathematical form as Eq. (17), i.e.,

$$\begin{aligned}S(\mathbf{r}_A) &= \int_{AP}\langle |E_0(\boldsymbol{\xi}_A)|^2\rangle\ \Phi(\boldsymbol{\xi}_A;\mathbf{r}_A;\lambda,z)\,d^2\xi_A\\ &\quad + 2\int_{AP} d^2\xi_A \int_{\substack{AP\\ \boldsymbol{\xi}_D\neq 0}} d^2\xi_D \langle |E_0(\boldsymbol{\xi}_+)|^2\rangle^{\frac{1}{2}}\langle |E_0(\boldsymbol{\xi}_-)|^2\rangle^{\frac{1}{2}}\\ &\quad \times \eta_0(\boldsymbol{\xi}_+,\boldsymbol{\xi}_-)\ \mathrm{Re}[\Phi(\boldsymbol{\xi}_+,\boldsymbol{\xi}_-;\mathbf{r}_A;\lambda,z)\langle \exp[i\,\beta_0(\boldsymbol{\xi}_+,\boldsymbol{\xi}_-)]\rangle],\end{aligned} \tag{20}$$

with $\mu(\boldsymbol{\xi}_+,\boldsymbol{\xi}_-) = \eta_0(\boldsymbol{\xi}_+,\boldsymbol{\xi}_-)\ \langle \exp[i\,\beta_0(\boldsymbol{\xi}_+,\boldsymbol{\xi}_-)]\rangle$ the complex degree of spatial coherence. Thus electric field vectors with uncorrelated amplitudes and/or random phase differences in the interval $[-\pi,\pi]$ make the wave field spatially incoherent without changing its linear polarization state. It occurs by the natural light emerging from a linear polarizer, like that used by Etienne Malus in his famous experiment performed in 1809 [5].

Equations (18) and (20) point out that natural light and linearly polarized light (parallel to the x axis), both spatially coherent to some extent, produce the same power spectrum at the OP. However, if the linear polarization states at $\boldsymbol{\xi}_\pm$ are mutually orthogonal, then $\vartheta(\boldsymbol{\xi}_-) = \vartheta(\boldsymbol{\xi}_+) \pm \pi/2$, $\mathbf{s}_0(\boldsymbol{\xi}_+,\boldsymbol{\xi}_-) = \mathbf{s}_1(\boldsymbol{\xi}_+,\boldsymbol{\xi}_-) = \delta(\boldsymbol{\xi}_D)$, and $\mathbf{s}_2(\boldsymbol{\xi}_+,\boldsymbol{\xi}_-) = \mathbf{s}_3(\boldsymbol{\xi}_+,\boldsymbol{\xi}_-) = 0$ stand, taking into account the randomness of the phase differences $\beta_{xy}(\boldsymbol{\xi}_+,\boldsymbol{\xi}_-)$ and $\beta_{yx}(\boldsymbol{\xi}_+,\boldsymbol{\xi}_-)$. As a consequence, Eq. (18) reduces to its first term and

$$S(\mathbf{r}_A) = \int_{AP}\langle\, |E_0(\boldsymbol{\xi}_A)|^2\rangle\ \Phi(\boldsymbol{\xi}_A;\mathbf{r}_A;\lambda,z)\,d^2\xi_A. \tag{21}$$

This means that mutually orthogonal linearly polarized states cannot interfere. Equations (20) and (21) are in accordance to the laws of interference and polarization established by Augustin-Jean Fresnel and Dominique-François-Jean Arago in 1819 [13].

Similar results are also straightforwardly obtained for linearly polarized light parallel to the y axis, by taking into account that the polarization angles of this type of light have narrow fluctuations around $\vartheta(\boldsymbol{\xi}_\pm) = \pi/2$, so that $\langle \cos\vartheta(\boldsymbol{\xi}_\pm)\rangle = 0$, $\langle \sin\vartheta(\boldsymbol{\xi}_\pm)\rangle = 1$, $\langle \cos\vartheta(\boldsymbol{\xi}_+)\,\cos\vartheta(\boldsymbol{\xi}_-)\rangle = 0$, $\langle \sin\vartheta(\boldsymbol{\xi}_+)\,\sin\vartheta(\boldsymbol{\xi}_-)\rangle = 1$, and $\langle \cos\vartheta(\boldsymbol{\xi}_\pm)\,\sin\vartheta(\boldsymbol{\xi}_\mp)\rangle = 0$ hold. In addition, Figs. 3–6 and their explanations are also valid for linearly polarized (parallel to any of the Cartesian axes) radiant point sources, if their polarization states are mutually parallel.

Let us consider the situation depicted in Fig. 7, in which the polarization state of the radiant point source at $\boldsymbol{\xi}_A = -2.5\lambda$ is turned orthogonal to the polarization states of the radiant point sources at $\boldsymbol{\xi}_A = 0,\ 2.5\lambda$. The mutually parallel polarized radiant point sources determine the space structure in graph (a), whose fringe number for $z = 8\lambda$ is more minor than the fringe number in Fig. 6, because the separation between the sources is shorter in this case than in the case of Fig. 6. The spatial link of such sources can be appreciated in profile (b), and the complete distribution of radiant point sources at the AP is reproduced by the main peaks of the profile (e), whose spreading is due to the Lorentzian envelope of the nonparaxial modes. Nevertheless, the fringe distribution determined by profile (c) is not centered at $x_A = 0$, and therefore the space structure for the transport of the power spectrum becomes asymmetric, as shown in the

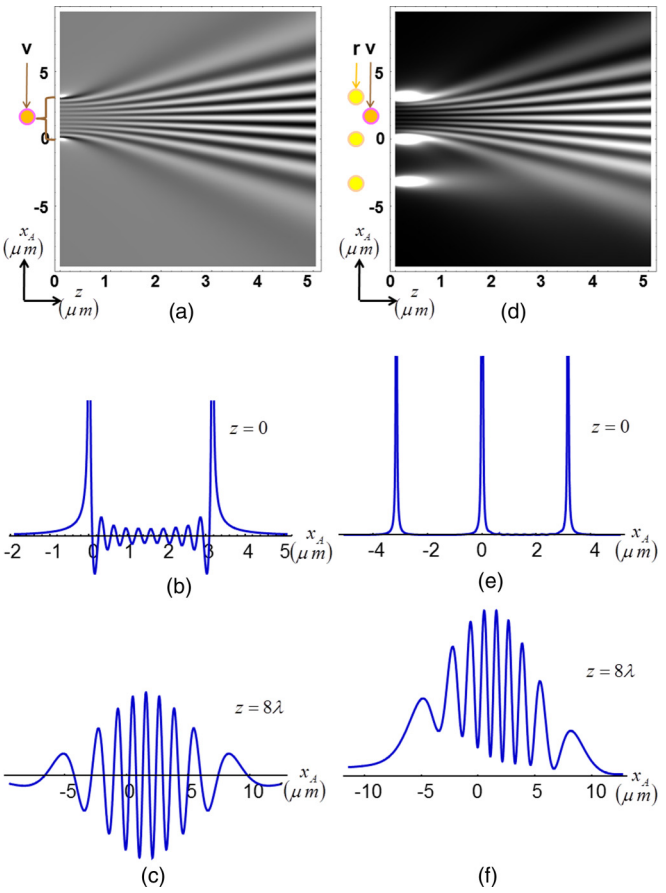

FIG. 7. (Color online) Transport of the electromagnetic wave field provided by the planar source in the examples before. The three radiant point sources are linearly polarized with null phase differences in between. The state of the source at $\boldsymbol{\xi}_A = -2.5\lambda$ is orthogonal to the states of the other two, which are mutually parallel. (a) Graph of the modulating power for $0 \leqslant z \leqslant 8\lambda$ ($\lambda = 0.632$ μm). (b, c) Profiles of the modulating power at specific propagation distances. (d) Graph of the power spectrum for $0 \leqslant z \leqslant 8\lambda$. (e, f) Profiles of the power spectrum at the same propagation distances as in (b) and (c), respectively.

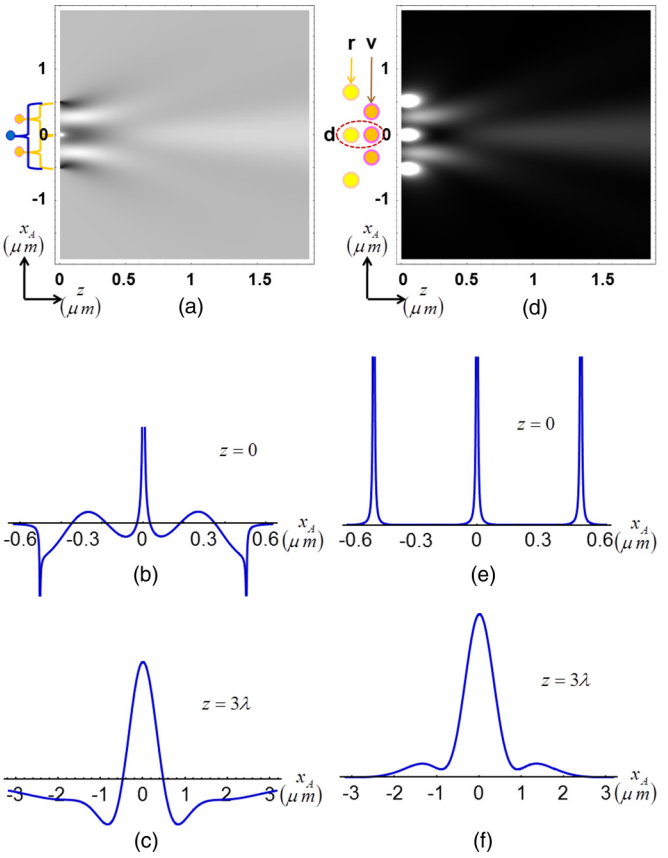

FIG. 8. (Color online) Transport of the electromagnetic wave field provided by the planar source in the examples before. The three radiant point sources are mutually parallel linearly polarized, with null phase differences and spacing 0.8λ. (a) Graph of the modulating power for $0 \leqslant z \leqslant 3\lambda$ ($\lambda = 0.632$ μm). (b, c) Profiles of the modulating power at specific propagation distances. (d) Graph of the power spectrum for $0 \leqslant z \leqslant 3\lambda$. (e, f) Profiles of the power spectrum at the same propagation distances as in (b) and (c), respectively.

graph (d). In addition, the fringe contrast diminishes because of the radiant power emitted by the source at $\boldsymbol{\xi}_A = -2.5\lambda$, as shown for $z = 8\lambda$ by profile (f).

It is worth noting that the differences between the behaviors illustrated by Figs. 5 and 7 are due to the polarization state exclusively, i.e., the complex degree of spatial coherence is equal to 1 in both of them. Thus, although this unified theory shows how the states of spatial coherence and polarization together determine the redistribution scheme of the total radiant power spectrum, their effects are clearly separated, i.e., the redistribution due to the spatial coherence state can be regarded as a scalar behavior in the sense that it is independent from the polarization state. The redistribution due to the polarization state should be regarded as a vector behavior, determined by the Fresnel-Arago interference and polarization laws applied to the pairs of radiant point sources within each structured support of spatial coherence.

This ability of the theoretical framework is very useful for analysis and modeling purposes, and quite different from the production of experimental results. Indeed, the physical attributes of the electromagnetic wave fields are usually nonseparable in the measurements of interference patterns, so that their separate identification in the experimental results is intricate and should require a priori information. The analysis above is also valid by subwavelength spacing of the radiant point sources, as illustrated by Figs. 8 and 9. In these examples, the three linearly polarized radiant point sources distribute with pitch 0.8λ, and their polarization states are mutually parallel in Fig. 8, while the polarization of the mid-source is turned orthogonal to the remaining sources in Fig. 9. Then, virtual point sources are placed at $\boldsymbol{\xi}_A = 0$ in the both cases but additional virtual point sources are turned on at $\boldsymbol{\xi}_A = \pm 0.4\lambda$ in Fig. 8. The graphs (a) of the both figures show the space structure due to the corresponding expansion of high-order modes, while the graphs (d) include the 0-order modes. Consequently, the cross sections of the graphs (d) correspond to the profiles of the power spectrum at planes transversal to the direction of propagation. Thus, the profiles (e) reproduce the distribution of the radiant point sources at the AP, whose spatial linkages are specified by the profiles (b), i.e. the three radiant point sources in Fig. 8

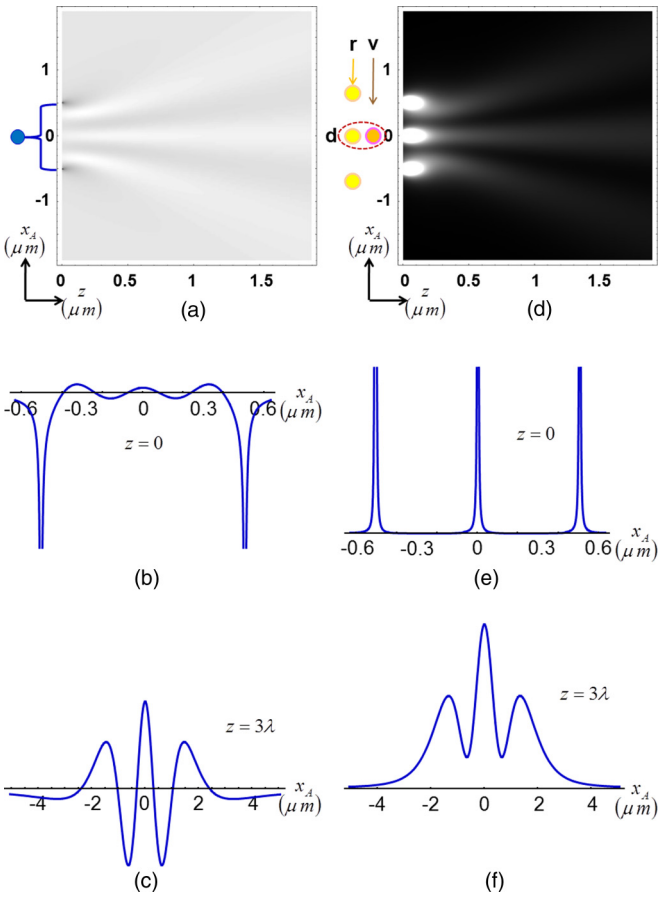

FIG. 9. (Color online) Transport of the electromagnetic wave field provided by the planar source in Fig. 8, but the polarization state of the mid-source was turned orthogonal to the polarization states of the other two. (a) Graph of the modulating power for $0 \leqslant z \leqslant 3\lambda$ ($\lambda = 0.632\ \mu$m). (b, c) Profiles of the modulating power at specific propagation distances. (d) Graph of the power spectrum for $0 \leqslant z \leqslant 3\lambda$. (e, f) Profiles of the power spectrum at the same propagation distances as in (b) and (c), respectively.

are correlated, while only the two with separation 1.6λ are correlated in Fig. 9. As before, the spreading of the main maxima of profiles (e) is due to the Lorentzian envelope of the nonparaxial modes. The profiles (b) and (e) significantly evolve in the microdiffraction domain, producing the profiles (c) and (f) for $z = 3\lambda$ respectively, i.e. diffraction patterns are configured in the microdiffraction domain, at the same propagation distances at which interference fringe patters are produced, when the pitch of the radiant point sources is 5λ. The effects of changing the polarization state of individual radiant point sources can be appreciated by comparing such profiles.

Therefore, this theoretical framework also unifies the description of interference and diffraction, characterizing them by the relationship between the spacing of the discrete set of radiant point sources and the scale metric λ. Specifically, $a > \lambda$, with a the spacing, is the interference condition, while $a \leqslant \lambda$ is the diffraction condition, provided $L > \lambda$, with L characterizing the size of the planar source [7,8]. Furthermore, all the examples above point out the three dimensional structure conferred to the power spectrum by the space structure of the volume delimited by the AP and the OP, with independence from the emission events of the planar source.

IV. THE SPATIAL COHERENCE STATE

It has also a three dimensional structure in the setup that significantly evolves in the microdiffraction domain. As discussed before, this state seems to be a scalar attribute of the electromagnetic wave field, and then it can be analyzed independently from the polarization state. To this aim, let us consider Eq. (1) for nonpolarized light in any state of spatial coherence, so that the electric cross-spectral density tensor becomes diagonal with elements

$$\mathbf{W}_{lm}(\mathbf{r}_+,\mathbf{r}_-) = \delta_{lm} \int_{AP} d^2\xi_A\ \mathbf{W}_{lm}(\boldsymbol{\xi}_A;\mathbf{r}_+,\mathbf{r}_-), \tag{22a}$$

where the suffices l,m stand for any combination of x, y and δ_{lm} is the Kronecker δ, and

$$\begin{aligned}
&\mathbf{W}_{xx}(\boldsymbol{\xi}_A;\mathbf{r}_+,\mathbf{r}_-) \\
&\quad = \mathbf{W}_{yy}(\boldsymbol{\xi}_A;\mathbf{r}_+,\mathbf{r}_-) \\
&\quad = \frac{1}{2} \int_{AP} d^2\xi_D\ \ \eta_0(\boldsymbol{\xi}_+,\boldsymbol{\xi}_-)\ \mathbf{s}_0(\boldsymbol{\xi}_+,\boldsymbol{\xi}_-) \langle |E_0(\boldsymbol{\xi}_+)|^2 \rangle^{\frac{1}{2}} \\
&\qquad \times \langle |E_0(\boldsymbol{\xi}_-)|^2 \rangle^{\frac{1}{2}}\ \Phi(\boldsymbol{\xi}_+,\boldsymbol{\xi}_-;\mathbf{r}_+,\mathbf{r}_-;\lambda,z),
\end{aligned} \tag{22b}$$

with $\mathbf{s}_0(\boldsymbol{\xi}_+,\boldsymbol{\xi}_-) = \langle \exp[i\,\beta_0(\boldsymbol{\xi}_+,\boldsymbol{\xi}_-)] \rangle$. Because $\mathbf{s}_{j>0}(\boldsymbol{\xi}_+,\boldsymbol{\xi}_-) = 0$ stands, then $\mathbf{P}(\boldsymbol{\xi}_A,\mathbf{r}_A) = 0$ holds too. Accordingly, the trace of the electric cross-spectral density tensor provides the nonparaxial description of the spatial coherence transport. It is a scalar description given by

$$\begin{aligned}
&\mathrm{Tr}[\mathbf{W}(\mathbf{r}_+,\mathbf{r}_-)] \\
&\quad = \mathrm{Tr}[\mathbf{W}(\mathbf{r}_+,\mathbf{r}_-)]_{\mathrm{rad}} + \mathrm{Tr}[\mathbf{W}(\mathbf{r}_+,\mathbf{r}_-)]_{\mathrm{vir}} \\
&\quad = \int_{AP} d^2\xi_A \langle |E_0(\boldsymbol{\xi}_A)|^2 \rangle\ \Phi(\boldsymbol{\xi}_A;\mathbf{r}_+,\mathbf{r}_-;\lambda,z) \\
&\qquad + 2 \int_{AP} d^2\xi_A \int_{\substack{AP \\ \boldsymbol{\xi}_D \neq 0}} d^2\xi_D\ \ \eta_0(\boldsymbol{\xi}_+,\boldsymbol{\xi}_-) \langle |E_0(\boldsymbol{\xi}_+)|^2 \rangle^{\frac{1}{2}} \\
&\qquad \times \langle |E_0(\boldsymbol{\xi}_-)|^2 \rangle^{\frac{1}{2}}\ \mathrm{Re}[\Phi(\boldsymbol{\xi}_+,\boldsymbol{\xi}_-;\mathbf{r}_+,\mathbf{r}_-;\lambda,z) \\
&\qquad \times \langle \exp[i\,\beta_0(\boldsymbol{\xi}_+,\boldsymbol{\xi}_-)] \rangle].
\end{aligned} \tag{23}$$

Accordingly, the state of spatial coherence of the electromagnetic wave field at the OP results from respective contributions of the radiant and the virtual sets of the planar source. Both terms should be regarded if the planar source is spatially coherent in some extent. However, the electromagnetic wave fields emitted by spatially incoherent planar sources become spatially partially coherent because of their transport to the OP [9]. This behavior implies strong variations of the spatial coherence state in the microdiffraction domain, formalized by only the radiant term of

Eq. (23), i.e.,

$$\mathrm{Tr}\,[\mathbf{W}(\mathbf{r}_+,\mathbf{r}_-)] = \mathrm{Tr}\,[\mathbf{W}(\mathbf{r}_+,\mathbf{r}_-)]_{\mathrm{rad}} = \int_{AP} d^2\xi_A\ \langle |E_0(\boldsymbol{\xi}_A)|^2\rangle\ \Phi(\boldsymbol{\xi}_A;\mathbf{r}_+,\mathbf{r}_-;\lambda,z) \tag{24a}$$

with

$$\Phi(\boldsymbol{\xi}_A;\mathbf{r}_+,\mathbf{r}_-;\lambda,z) = \left(\frac{k}{4\pi}\right)^2 t(\boldsymbol{\xi}_+)\,t^*(\boldsymbol{\xi}_-)\left(\frac{z+|\,\mathbf{z}+\mathbf{r}_A-\boldsymbol{\xi}_A+\mathbf{r}_D/2\,|}{|\,\mathbf{z}+\mathbf{r}_A-\boldsymbol{\xi}_A+\mathbf{r}_D/2\,|^2}\right)\left(\frac{z+|\,\mathbf{z}+\mathbf{r}_A-\boldsymbol{\xi}_A-\mathbf{r}_D/2\,|}{|\,\mathbf{z}+\mathbf{r}_A-\boldsymbol{\xi}_A-\mathbf{r}_D/2\,|^2}\right)$$
$$\times \exp(i\,k\,|\,\mathbf{z}+\mathbf{r}_A-\boldsymbol{\xi}_A+\mathbf{r}_D/2\,|-i\,k\,|\,\mathbf{z}+\mathbf{r}_A-\boldsymbol{\xi}_A-\mathbf{r}_D/2\,|). \tag{24b}$$

Therefore, the modal expansion in Eq. (24a) determines the transport of the radiant set contribution to the spatial coherence state over the structured supports centered at each $\mathbf{r}_A$ on the OP. It is worth noting that the expansion length (i.e. the size of the integration region) is determined by the size of the planar source. In other words, the gain in spatial coherence is mainly a spatial effect, in which the nonparaxial modes are chosen by the geometry of the planar source and weighted by the average electric power distribution across it. Eq. (24a) leads to the Van Cittert–Zernike theorem [2,5] by assuming propagation in the paraxial region of the far field.

The graphs of Fig. 10 illustrate the magnitude and the phase of Eq. (24a) by assuming a uniform and homogeneous planar source composed by 11 uncorrelated identical radiant point sources, regularly arranged under diffraction condition (pitch $\lambda/2$). The graphs show the evolution of the structured support centered at $x_A = 0$. The fringe structure of the phase

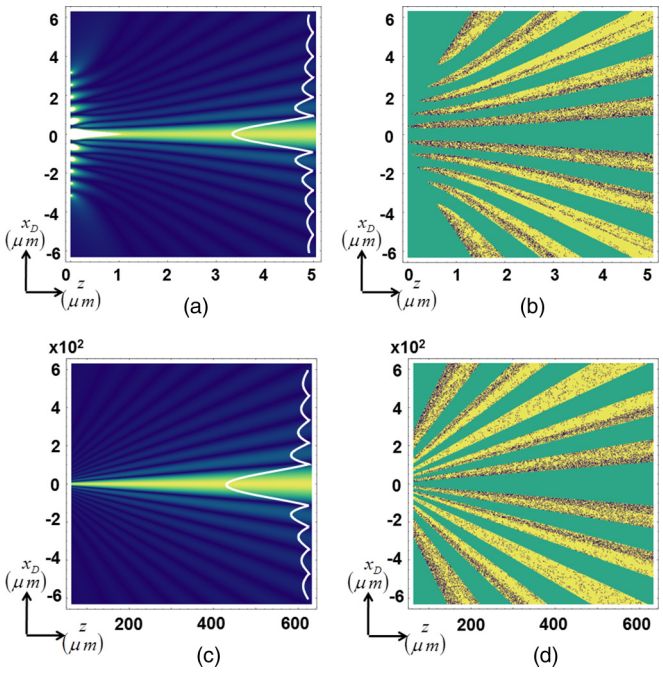

FIG. 10. (Color online) Graphs of Eq. (24a) for the structured support centered at $x_A = 0$. The spatially incoherent planar source is a line of 11 identical radiant point sources with pitch $\lambda/2$, at the scale metric $\lambda = 0.632$ μm. (a) Magnitude and (b) phase for $0 \leqslant z \leqslant 8\lambda$; the same quantities are shown in (c) and (d), respectively, for $10^2\lambda \leqslant z \leqslant 10^3\lambda$. The graphs in (a) and (c) are enhanced for presentation purposes.

graphs points out phase changes between the values 0 and $\pm\pi$. It means that $\mathrm{Tr}[\mathbf{W}(x_D)]$ is real valued with sign changes between consecutive lobes in this case. The contributions of the individual point sources are resolved at very short distance z, and evolve to an invariant shape even in the microdiffraction domain. This shape exhibits a central main maximum and secondary lateral maxima that decreases monotonically. The support of the main maximum, delimited by the first lateral zeroes, defines the structured support of spatial coherence. Its growth along the z axis is apparent in the graphs (a) and (c).

The shape invariance of the structured support across the OP at a specific propagation distance is illustrated in Fig. 11, for the same planar source and scale metric as in Fig. 10. The graphs (a) in both figures are quite different to each other, but the graphs in Figs. 10(c) and 11(b) become similar as the distance z increases. This means that not only the axial variations of the spatial coherence state are significant in the microdiffraction domain, but also the transversal variations. However, the structured support becomes both axially and transversally shape invariant in the far field.

Thus there should be a region around the z axis at each specific propagation distance, in which the structured supports of spatial coherence produced by any uniform and homogeneous planar source are equally shaped, as predicted by the Van Cittert–Zernike theorem for the paraxial region in the far field.

V. PARAXIAL VALIDATION

The predictions of this theory have not yet been directly validated by experimentation because of strong technological constraints. Nevertheless, its consistency can be well

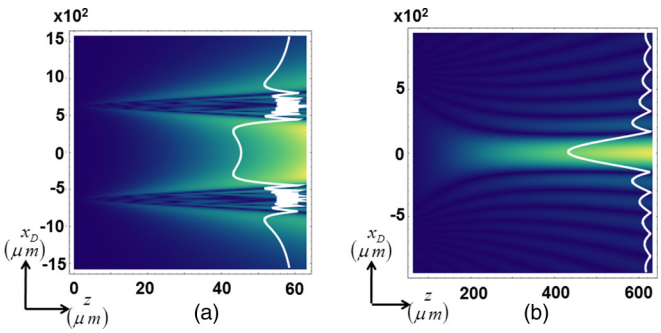

FIG. 11. (Color online) Graphs of Eq. (24a) for the structured support centered at $x_A = 500\lambda$ on the OP, provided by the same planar source in Fig. 10 for (a) $0 \leqslant z \leqslant 10^2\lambda$ and (b) $10^2\lambda \leqslant z \leqslant 10^3\lambda$. The graphs are enhanced for presentation purposes.

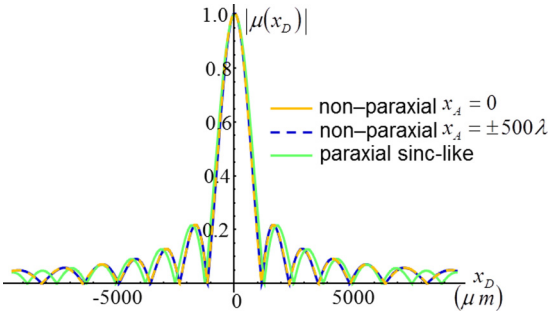

FIG. 12. (Color online) Profiles of the moduli of the degree of spatial coherence in Figs. 10 and 11, and of the paraxial approached sinclike degree for $10^4\lambda \leqslant z \leqslant 10^6\lambda$, i.e., such profiles remain invariant along this propagation segment.

established by showing its ability to predict well-known experimental results for the paraxial segment in the far-field propagation.

For instance, under this approach the Van Cittert–Zernike theorem predicts a sinclike degree of spatial coherence at the OP, for the electromagnetic field emitted by a slit uniformly illuminated. This prediction has been validated by experimental results [5], particularly for the main maximum that defines the spatial coherence support, and the first two lateral lobes. (The spatial coherence in these lobes is usually neglected in practical applications.)

The profiles in Fig. 12 allow comparing the moduli of the nonparaxial degree of spatial coherence in Figs. 10 and 11 with the modulus of the paraxial sinclike degree, by regarding a slit of width equal to the length of the radiant point source arrangement, i.e., 5λ ($\lambda = 0.632\ \mu$m). As expected, the exact nonparaxial profiles are identical to each other and remain invariant along the propagation segment $10^4\lambda \leqslant z \leqslant 10^6\lambda$. The paraxial approached sinclike profile fits well the exact profiles until the fourth lateral lobe. Thus, according to the experimental criteria for determining the spatial coherence state of the electromagnetic wave field [5], Fig. 12 leads to the conclusion that the paraxial approached version of the Van Cittert–Zernike theorem provides an accurate approximation for the far-field propagation.

Profiles in Fig. 13 point out the validity of the interference condition and the effect of the polarization states of the radiant point sources on the interference pattern. Three identical, spatially coherent, and linearly polarized radiant point sources are considered. The paraxial approached prediction significantly fit the exact nonparaxial predictions for longer enough spacing of the radiant point sources, as shown in profiles (b) and (d). Such profiles are confirmed by experimental results. However, if the spacing is comparable to the wavelength, the paraxial approached prediction significantly deviates from the exact nonparaxial prediction, as shown in profiles (a) and (c). The deviation is due to the Lorentzian envelope and the spatial frequency chirping of the nonparaxial patterns that cannot be predicted by the paraxial approach. Nevertheless, both types of predictions coincide in the shapes of the interference patterns, i.e., high contrasted main maxima with only one weak secondary maximum in between if the polarization states of the radiant point sources are mutually parallel.

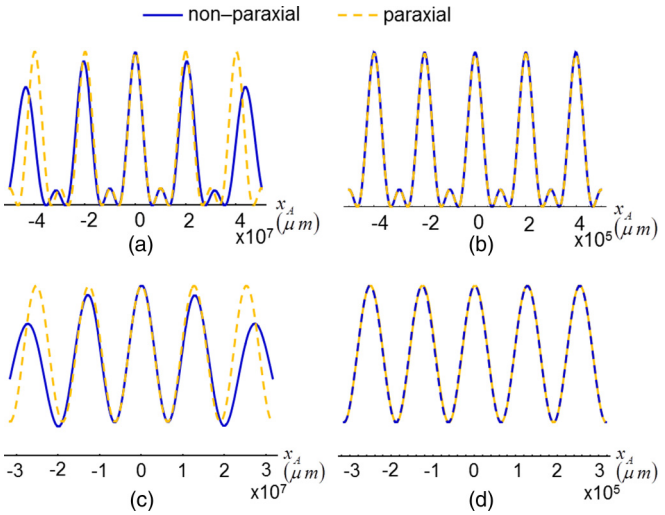

FIG. 13. (Color online) Profiles of the interference patterns produced by three identical, spatially coherent, and linearly polarized radiant point sources in the far field ($z = 10^8\lambda$, $\lambda = 0.632\,\mu$m). (a) Mutually parallel polarization states and spacing 5λ. (b) Mutually parallel polarization states and spacing 500λ. The state of the source at $\boldsymbol{\xi}_A = -2.5\lambda$ is turned orthogonal to the states of the other two in (c) and (d), and the spacing is the same as in (a) and (b), respectively.

These patterns turn to relatively low–contrasted, cosinelike interference patterns as the polarization state of the radiant point source at $\boldsymbol{\xi}_A = -2.5\lambda$ is turned orthogonal to the other two. The spatial frequency of the pattern is determined by the mutually parallel polarized sources, and the contrast loss is due to the radiant power emitted by the source at $\boldsymbol{\xi}_A = -2.5\lambda$. Because of the short length of the considered segment, the asymmetry of the profile (f) in Fig. 7 cannot be appreciated. In summary, the experimental supported predictions of the paraxial approached model appear as cases under specific conditions of the exact nonparaxial formulation.

Figure 14 allows comparing the far-field diffraction profiles ($z = 10^4\mu$m) predicted by the exact nonparaxial formulation and the paraxial approached model. Linear arrays of point sources are regarded for the former one, while slits of width equal to the length of the corresponding point source array are considered for the last one. Both types of predictions point out the validity of the diffraction condition, and their

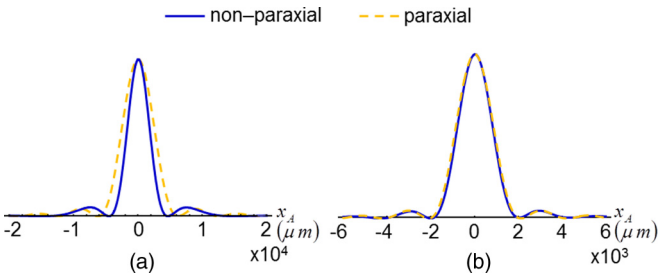

FIG. 14. (Color online) Profiles of the diffraction patterns produced by identical, spatially coherent, and mutually parallel, linearly polarized radiant point sources in the far field ($z = 10^4\ \mu$m). The exact nonparaxial pattern is provided by three sources with spacing 0.8λ in (a) and by 16 sources with spacing 0.3λ in (b) ($\lambda = 0.632\,\mu$m). The paraxial approached pattern is provided by a slit of width 1.6λ in (a) and 4.5λ in (b).

fit is significantly good if the density of radiant point sources of the planar source is high enough, as shown by profiles (b). In this case, the profiles exhibit squared, sinclike shapes, as reported by basic optics experiments. However, the paraxial approached prediction significantly deviates from the exact nonparaxial prediction under more strong restrictions of the microdiffraction, like few radiant point sources with subwavelength spacing, as illustrated by profiles (a). Once more, the experimental supported predictions of the paraxial approached model appear as cases under specific conditions of the exact nonparaxial formulation.

The comparisons above point out that the Wigner optics formulation (also called the Wigner phase-space representation) is not suitable in the microdiffraction domain. Wigner optics [11] is widely used at the present because of the versatility and efficiency of its Fourier methods for partially coherent wave fields, as well as the accepted physical meanings of their parameters. However, its accuracy is limited to the paraxial approach in the far-field propagation. For the microdiffraction domain, the exact predictions of the theory proposed in this work seem to be required. This formulation is consistent with the experimental supported paraxial predictions, but novel physical attributes should be conferred to the electromagnetic wave field in order to apply it rigorously.

VI. SUMMARY AND CONCLUSION

The presented theory provides a unified framework for the transport of the power and the states of spatial coherence and polarization of electromagnetic wave fields, as well as for diffraction and interference, in the microdiffraction domain. The accuracy of the theory is assured by its exact nonparaxial formulation, and its versatility is assured by a precise separation of the physical and the spatial features. In this sense, nonparaxial modes, determined only by the boundary conditions of the experimental setups, establish a spatial structure between the aperture and the observation planes that is independent of the physical features of the planar source. They are deterministic scalar functions, in contrast to the physical source attributes which are formalized by tensors of statistical nature. Furthermore, the theory characterizes any planar source in terms of inserted sets of radiant and virtual point sources, whose emissions are of a different nature and are transported by nonparaxial modes of different orders.

The theory is consistent with the classical optical laws as well as with the experimental supported paraxial predictions, which appear as particular cases. It also overcomes the limitations of the conventional paraxial theories in the microdiffraction domain, being able to predict the strong changes suffered by the electromagnetic wave field in this domain.

ACKNOWLEDGMENTS

This work was partially supported by the Patrimonio Autónomo Fondo Nacional de Financiamiento para la Ciencia, la Tecnología y la Innovación, Francisco José de Caldas, Colciencias Grant No. 111852128322, and by the Universidad Nacional de Colombia, Vicerrectoría de Investigación, Grants No. 12932 and No. 12934.

APPENDIX

This Appendix concerns the deduction of Eq. (1). The elements of the electric cross-spectral density tensor are given by the Wolf's integral equation [2],

$$W_{lm}(\mathbf{r}_+,\mathbf{r}_-) = \left(\frac{k}{4\pi}\right)^2 \int_{AP}\int_{AP} d^2\xi_D\, d^2\xi_A\;\; W_{lm}(\boldsymbol{\xi}_+,\boldsymbol{\xi}_-)\, t(\boldsymbol{\xi}_+)\, t^*(\boldsymbol{\xi}_-)$$
$$\times \left(\frac{z + |\,\mathbf{z}+\mathbf{r}_A-\boldsymbol{\xi}_A+(\mathbf{r}_D-\boldsymbol{\xi}_D)/2|}{|\,\mathbf{z}+\mathbf{r}_A-\boldsymbol{\xi}_A+(\mathbf{r}_D-\boldsymbol{\xi}_D)/2\,|^2}\right)\left(\frac{z + |\,\mathbf{z}+\mathbf{r}_A-\boldsymbol{\xi}_A-(\mathbf{r}_D-\boldsymbol{\xi}_D)/2|}{|\,\mathbf{z}+\mathbf{r}_A-\boldsymbol{\xi}_A-(\mathbf{r}_D-\boldsymbol{\xi}_D)/2\,|^2}\right)$$
$$\times \exp(i\,k\,|\,\mathbf{z}+\mathbf{r}_A-\boldsymbol{\xi}_A+(\mathbf{r}_D-\boldsymbol{\xi}_D)/2\,| - i\,k\,|\,\mathbf{z}+\mathbf{r}_A-\boldsymbol{\xi}_A-(\mathbf{r}_D-\boldsymbol{\xi}_D)/2\,|), \tag{A1}$$

where l, m stand for any combination of x, y, so that $W_{lm}(\boldsymbol{\xi}_+,\boldsymbol{\xi}_-) = \langle E_l(\boldsymbol{\xi}_+)\, E_m^*(\boldsymbol{\xi}_-)\rangle$ and $W_{lm}(\mathbf{r}_+,\mathbf{r}_-) = \langle E_l(\mathbf{r}_+)\, E_m^*(\mathbf{r}_-)\rangle$ represent the correlations of the Cartesian components of the electric field vectors at the AP and the OP, respectively. The angular parenthesis and the asterisk denote ensemble average [2] and complex conjugate, respectively.

Furthermore, $E_l(\boldsymbol{\xi}_\pm) = E_0(\boldsymbol{\xi}_\pm)\, \psi_l(\vartheta(\boldsymbol{\xi}_\pm))\exp[i\varepsilon_l(\boldsymbol{\xi}_\pm)]$, with $E_0(\boldsymbol{\xi}_\pm)$ the magnitude of the electric field vector, $\varepsilon_l(\boldsymbol{\xi}_\pm)$ its phase, and $\vartheta(\boldsymbol{\xi}_\pm)$ its polarization angle with respect to the x axis, so that $\psi_x(\vartheta(\boldsymbol{\xi}_\pm)) = \cos\vartheta(\boldsymbol{\xi}_\pm)$ and $\psi_y(\vartheta(\boldsymbol{\xi}_\pm)) = \sin\vartheta(\boldsymbol{\xi}_\pm)$ are the polarization functions [3]. This theory concerns random stationary electromagnetic fields, for which the amplitude of the electric field vector, its phase, and its polarization angle are statistically independent variables to each other, because the first two depend on the complex amplitude fluctuations of the field while the third depends on its polarization fluctuations referred to a specific choice of coordinate axes [2,13]. Therefore

$$W_{lm}(\boldsymbol{\xi}_+,\boldsymbol{\xi}_-) = \langle E_0(\boldsymbol{\xi}_+)\, E_0(\boldsymbol{\xi}_-)\rangle\langle\psi_l(\vartheta(\boldsymbol{\xi}_+))\,\psi_m(\vartheta(\boldsymbol{\xi}_-))\rangle$$
$$\times \langle\exp[i\varepsilon_l(\boldsymbol{\xi}_+) - i\varepsilon_m(\boldsymbol{\xi}_-)]\rangle \tag{A2}$$

stands. Now, let us take into account the following expressions:

$$\langle E_0(\boldsymbol{\xi}_+)\, E_0(\boldsymbol{\xi}_-)\rangle = \langle\,|E_0(\boldsymbol{\xi}_+)|^2\rangle^{\frac{1}{2}}\,\langle\,|E_0(\boldsymbol{\xi}_-)|^2\rangle^{\frac{1}{2}}\,\eta_0(\boldsymbol{\xi}_+,\boldsymbol{\xi}_-), \tag{A3}$$

with $\eta_0(\boldsymbol{\xi}_+,\boldsymbol{\xi}_-) = \langle E_0(\boldsymbol{\xi}_+)\, E_0(\boldsymbol{\xi}_-)\rangle/\langle E_0^2(\boldsymbol{\xi}_+)\rangle^{\frac{1}{2}}\,\langle\, E_0^2(\boldsymbol{\xi}_-)\rangle^{\frac{1}{2}}$ a real valued quantity that takes values only into the interval [0, 1],

$$\boldsymbol{\Psi}_{lm}(\boldsymbol{\xi}_\pm) = \left\langle\psi_l^2(\vartheta(\boldsymbol{\xi}_\pm))\right\rangle^{\frac{1}{2}}\,\delta_{lm}, \tag{A4}$$

with δ_{lm} the Kronecker δ, and

$$\boldsymbol{\eta}_{lm}(\boldsymbol{\xi}_+,\boldsymbol{\xi}_-) = \eta_0(\boldsymbol{\xi}_+,\boldsymbol{\xi}_-)\,\Theta_{lm}(\boldsymbol{\xi}_+,\boldsymbol{\xi}_-)\,\langle \exp[\,i\,\beta_{lm}(\boldsymbol{\xi}_+,\boldsymbol{\xi}_-)\,]\,\rangle \tag{A5}$$

the spatial coherence-polarization tensor, with $\beta_{lm}(\boldsymbol{\xi}_+,\boldsymbol{\xi}_-) = \varepsilon_l(\boldsymbol{\xi}_+) - \varepsilon_m(\boldsymbol{\xi}_-)$ and

$$\Theta_{lm}(\boldsymbol{\xi}_+,\boldsymbol{\xi}_-) = \langle \psi_l(\vartheta(\boldsymbol{\xi}_+))\,\psi_m(\vartheta(\boldsymbol{\xi}_-))\rangle \Big/ \left\langle \psi_l^2(\vartheta(\boldsymbol{\xi}_+))\right\rangle^{\frac{1}{2}} \left\langle \psi_m^2(\vartheta(\boldsymbol{\xi}_-))\right\rangle^{\frac{1}{2}}$$

a real valued quantity that takes values only into the interval [0, 1]. By regarding $\eta_0(\boldsymbol{\xi}_+,\boldsymbol{\xi}_-) = \eta_0(\boldsymbol{\xi}_-,\boldsymbol{\xi}_+)$, $\Theta_{lm}(\boldsymbol{\xi}_+,\boldsymbol{\xi}_-) = \Theta_{ml}(\boldsymbol{\xi}_-,\boldsymbol{\xi}_+)$, and $\beta_{lm}(\boldsymbol{\xi}_+,\boldsymbol{\xi}_-) = -\beta_{ml}(\boldsymbol{\xi}_-,\boldsymbol{\xi}_+)$, then $\boldsymbol{\eta}_{lm}(\boldsymbol{\xi}_+,\boldsymbol{\xi}_-) = \boldsymbol{\eta}^*_{ml}(\boldsymbol{\xi}_-,\boldsymbol{\xi}_+)$ holds, i.e., the spatial coherence-polarization tensor is Hermitian. It is worth regarding that $0 \leqslant |\boldsymbol{\eta}_{lm}(\boldsymbol{\xi}_+,\boldsymbol{\xi}_-)| \leqslant 1$ holds, with $|\boldsymbol{\eta}_{lm}(\boldsymbol{\xi}_+,\boldsymbol{\xi}_-)| = 1$ for highly correlated electromagnetic wave fields in both the electric field vector amplitudes and their polarization angles, and with deterministic phase differences, while $|\,\boldsymbol{\eta}_{lm}(\boldsymbol{\xi}_+,\boldsymbol{\xi}_-)\,| = 0$ if the field amplitudes or polarization angles are uncorrelated or the phase differences randomly fluctuate. Partially correlated fields with quasideterministic phase differences are characterized by $0 < |\,\boldsymbol{\eta}_{lm}(\boldsymbol{\xi}_+,\boldsymbol{\xi}_-)\,| < 1$.

Equations (A3)–(A5) allow expressing the 2×2 electric cross-spectral density tensor of elements $W_{lm}(\boldsymbol{\xi}_+,\boldsymbol{\xi}_-)$ [Eq. (A2)] as

$$\mathbf{W}(\boldsymbol{\xi}_+,\boldsymbol{\xi}_-) = \langle\,|E_0(\boldsymbol{\xi}_+)\,|^2\rangle^{\frac{1}{2}}\;\langle\,|E_0(\boldsymbol{\xi}_-)\,|^2\rangle^{\frac{1}{2}} \times \boldsymbol{\Psi}(\boldsymbol{\xi}_+)\,\boldsymbol{\eta}(\boldsymbol{\xi}_+,\boldsymbol{\xi}_-)\,\boldsymbol{\Psi}(\boldsymbol{\xi}_-). \tag{A6}$$

So, Eqs. (A1)–(A6) yield Eq. (1).

[1] S. Guha and G. Gillen, Opt. Express **13**, 1424 (2005).

[2] L. Mandel and E. Wolf, *Optical Coherence and Quantum Optics* (Cambridge University Press, Cambridge, MA, 1995), Eq. (4.4-25) is the Wolf's integral equation.

[3] R. Castañeda, Opt. Commun. **284**, 4114 (2011).

[4] R. Castañeda and H. Muñoz, Opt. Express **21**, 11276 (2013).

[5] M. Born and E. Wolf, *Principles of Optics*, 6th ed. (Pergamon Press, Oxford, 1993).

[6] R. Castañeda, H. Muñoz-Ossa, and G. Cañas-Cardona, J. Mod. Opt. **58**, 962 (2011).

[7] R. Castañeda, D. Vargas, and E. Franco, Opt. Express **21**, 12964 (2013)

[8] R. Castañeda, E. Franco, and D. Vargas, Phys. Scripta **88**, 035401 (2013).

[9] The gain in spatial coherence by spatially incoherent fields due only to their propagation was first established for the paraxial approach in the far-field domain by the celebrated Van Cittert–Zernike theorem, as reported in [2]. It was originally reported in P. H. Van Cittert, Physica **1**, 201 (1934); **6**, 1129 (1939); F. Zernike, *ibid.* **5**, 785 (1938).

[10] R. Castañeda, Opt. Commun. **284**, 4259 (2011).

[11] M. Testorf, B. Hennelly, and J. Ojeda-Castaneda, *Phase-Space Optics: Fundamentals and Applications* (McGraw-Hill, New York, 2010).

[12] E. Wolf, *Introduction to the Theory of Coherence and Polarization of Light* (Cambridge University Press, Cambridge, UK, 2007).

[13] M. Mujat, A. Dogariu, and E. Wolf, J. Opt. Soc. Am. A **21**, 2414 (2004).